Intrinsic precursors and timescale of the tropical Indian Ocean Dipole: Insights from partially decoupled numerical experiments

Julien Crétat[1]*, Pascal Terray[1,2], Sébastien Masson[1], K P Sooraj[3]

[1] *Sorbonne Universités (UPMC, Univ Paris 06)-CNRS-IRD-MNHN, LOCEAN Laboratory, IPSL, Paris, France*

[2] *Indo-French Cell for Water Sciences, IISc-NIO-IITM–IRD Joint International Laboratory, IITM, Pune, India*

[3] *Centre for Climate Change Research, Indian Institute of Tropical Meteorology, Pune, India*

Submitted to Climate Dynamics

06/15/2017

* Corresponding author address: Julien Crétat

julien.cretat@locean-ipsl.upmc.fr

Abstract

The intrinsic precursors and timescale of the tropical Indian Ocean Dipole (IOD) are examined with the help of a partially coupled global experiment with decoupled SST over the tropical Pacific.

The IOD does exist in the absence of El Niño Southern Oscillation (ENSO) in our modeling framework, but has weaker amplitude and damped Bjerknes feedback. However, IOD variability is much more biennial in the absence than presence of ENSO, especially in the eastern equatorial Indian Ocean (IO). Such biennial rhythm results mainly from two mechanisms internal to the IO.

The tropical ocean dynamics play a key role in the biennial anomalies during boreal winter with a sudden reversal of thermocline anomalies in the eastern equatorial IO forced by intraseasonal disturbances reminiscent of the Madden-Julian Oscillation (MJO). Such preconditioning is stronger after the occurrence of negative IOD events during the preceding boreal fall, underlying two-way interactions between IOD and MJO and asymmetry in this relationship. However, this preconditioning is not sufficient for triggering IOD events in the next boreal spring *per se*.

The main trigger for pure IODs relates to tropical-extratropical interactions within the IO, Convection and diabating heating associated with negative IODs promote a Gill-type tropical response, excite mid-latitude wave-trains and subtropical blocking in the Southern Hemisphere that trigger positive subtropical IOD events during boreal winter. The latter

promotes cold SST and anticyclonic circulation anomalies over the southeast IO that persist and migrate northeastward, triggering positive IOD events during the next boreal spring.

Accounting for the complementary influence of tropical ocean dynamics coupled to MJO and tropical-extratropical ocean-atmosphere interactions may thus help improving IOD predictability.

Keywords: biennial variability – coupled climate model – Indian Ocean Dipole – MJO – ocean dynamics – tropical-extratropical interactions

1. Introduction

The Indian Ocean Dipole (IOD) is an important ocean–atmosphere coupled mode of variability in the Indian Ocean (IO; Saji et al. 1999; Webster et al. 1999; Schott et al. 2009). Positive IOD events (pIODs) are associated with cool SST and shallow thermocline in the eastern IO, and warm SST and deep thermocline in its western part. The reverse holds for negative IOD events (nIODs). The IOD typically initiates during boreal spring and peaks in September-November (SON) in relation to wind–thermocline–Sea Surface Temperature (SST) and wind–evaporation–SST feedbacks (Annamalai et al. 2003; Li et al. 2003; Fischer et al. 2005; Spencer et al. 2005; Terray et al. 2007; Schott et al. 2009; Wang and Wang 2014). The former feedback known as the Bjerknes feedback, materializes positive coupled interactions between zonal wind, SST and thermocline anomalies over the equatorial IO during boreal fall and plays a central role in the IOD amplitude and length in both observations and current coupled models (Schott et al. 2009; Liu et al. 2014). The IOD significantly modulates rainfall interannual variability of surrounding (e.g., Ashok et al. 2003; Black et al. 2003; Gadgil et al. 2004; Behera et al. 2005; Ummenhofer et al. 2009; Krishnaswamy et al. 2015) and remote (e.g., Saji and Yamagata 2003; Yamagata et al. 2004; Chan et al. 2008; Cai et al. 2011) regions. Predicting IOD is thus of primary importance for improving our ability in seasonal rainfall forecasting. However, IOD prediction skill remains very limited and much shorter than the one associated with El Niño Southern Oscillation (ENSO, Shi et al. 2012; Liu et al. 2016).

Developing El Niños frequently trigger pIODs by inducing subsidence in the eastern equatorial IO, low-level anticyclonic circulation over the southeastern IO and upwelling-favorable winds off Java–Sumatra (Annamalai et al. 2003; Gualdi et al. 2003; Shinoda et al.

2004a-b; Fischer et al. 2005; Yu and Lau 2005; Behera et al. 2006; Schott et al. 2009; Hong et al. 2010; Guo et al. 2015). This scenario reverses during developing La Niñas and stands for most ENSO events, except some ENSO Modoki events (Wang and Wang 2014). Guo et al. (2015) have suggested that the IO basinwide mode induced by ENSO (Klein et al. 1999; Lau and Nath 2003; Schott et al. 2009) might also influence on IOD variability through generation of anomalous off-equatorial ocean Rossby waves and their effects on the western IO (Schott et al. 2009).

Many additional tropical mechanisms have also been proposed as potential triggers for IOD (Kajikawa et al. 2003; Fischer et al. 2005; Drbohlav et al. 2007; Yan and Liu 2009; Guo et al. 2013, 2015; Sun et al. 2015; Wang et al. 2016). Meehl et al. (2003), Drbohlav et al. (2007) and Sun et al. (2015) underline the role of the Indian Summer Monsoon (ISM) circulation in warming the western IO and cooling the eastern tropical IO during boreal summer. Another potential trigger for IOD involves boreal spring convection over Indonesia and the western Pacific (Kajikawa et al. 2003; Hendon 2003; Wang et al. 2016), with above (below) than normal convection driving westerly (easterly) wind anomalies over the equatorial IO that trigger nIODs (pIODs). Yan and Liu (2009) also suggest that the intra-seasonal atmospheric forcing such as, the Madden–Julian oscillation (MJO), plays a significant role in IOD triggering. In addition, the relationships between the Indonesian Throughflow, IOD and ENSO have also been highlighted (Tozuka et al. 2007; Yuan et al. 2011; Sprintall and Revelard 2014).

The extratropical IO is another important potential trigger for IOD (Terray et al. 2005, 2007; Fischer et al. 2005; Guo et al. 2015). Pure IODs can be triggered by anomalous winds along the Java-Sumatra coast (Fischer et al. 2005; Guo et al. 2015). These southeasterly winds relate

111 to intensification of the Mascarene High (Terray et al. 2005) that force the so-called
112 Subtropical IO Dipole (SIOD) during the previous boreal winter and spring (Behera and
113 Yamagata 2001; Suzuki et al. 2004; Morioka et al. 2012). During its positive phase, the cold
114 SST anomalies in the eastern SIOD pole favor a regional anticyclonic anomalous circulation
115 and upwelling-favorable winds off Java-Sumatra (Fischer et al. 2005; Terray et al. 2007).
116
117 In addition, oceanic dynamics within the IO have been shown to be critical for IOD triggering
118 and termination (Murtugudde et al. 2000; Feng and Meyers 2003; Shinoda et al. 2004b; Rao
119 and Behera 2005; Rao et al. 2009; McPhaden and Nagura 2014). IOD variability depicts
120 many features of the delayed oscillator theory (Webster et al. 1999; Murtugudde et al. 2000;
121 Feng and Meyers 2003; Yamagata et al. 2004; Rao and Behera 2005; Yuan and Liu 2009;
122 Wang and Yuan 2015) and recharge oscillator theory (McPhaden and Nagura 2014)
123 traditionally developed for understanding ENSO (Battisti and Hirst 1989; Jin 1997). This
124 implies that wind-forced oceanic waves in the IO and their western and eastern boundary
125 reflections are important to predict the surface dipole independently from ENSO (Wang and
126 Yuan 2015; McPhaden and Nagura 2014; Delman et al. 2016). Boreal spring anomalous
127 anticyclonic circulation off Java-Sumatra forces equatorial upwelling Kelvin waves, which
128 are essential for SST cooling along Java and pIOD triggering during boreal spring (Delman et
129 al. 2016). Such anomalous atmospheric circulation also generates equatorial and off-
130 equatorial downwelling Rossby waves, which can reflect at the western boundary of the IO
131 into downwelling equatorial Kelvin waves, helping terminating pIODs and promoting
132 favorable conditions for nIOD development during the following year (Rao et al. 2002, 2005;
133 Feng and Meyers 2003; Yuan and Liu 2009).
134
135 This review illustrates that IOD can be triggered by a large variety of local and remote

phenomena. The extent to which many of these IOD precursors are independent of ENSO is, however, hardly quantifiable in most studies since they make use of observations or models that contain ENSO variability. Recently, Stuecker et al. (2017) argue that IOD and its biennial timescale can be fully explained by ENSO and the seasonal modulation of ocean-atmosphere feedbacks over the Indo-Pacific region without any significant ocean memory in the IO, thus reactivating the old debate on the nature of IOD variability (Schott et al. 2009). A way to clarify the intrinsic IOD predictors and timescale (e.g., biennial variability), without any interference with ENSO, is using coupled ocean-atmosphere simulations with partial decoupling over the tropical Pacific to forbid ENSO development and variability. Such approach has been successfully used for analyzing the roles of Indian and Atlantic Oceans on ENSO (Luo et al. 2010; Santoso et al. 2012; Terray et al. 2016; Kajtar et al. 2016), the impact of SST errors on ISM (Prodhomme et al. 2014), the two-way relationship between IOD and ISM (Crétat et al. 2016), and the IOD and its forcing mechanisms in the absence of ENSO (Fischer et al. 2005; Behera et al. 2006; Yang et al. 2015; Wang et al. 2016; Stuecker et al. 2017). Here, this methodology is used to re-examine intrinsic IOD precursors and timescale, if any, in the absence of ENSO.

The paper is organized as follows. Section 2 presents the observations, the model experiments, and the methodology used. Section 3 is model validation and discusses the basic effects of ENSO removing on IOD during its peak and the associated Bjerknes feedback. Section 4 identifies the main precursors for IOD in both the presence and absence of ENSO. Section 5 focuses on the IOD timescale in the absence of ENSO, including the role of ocean dynamics, MJO and tropical-extratropical interactions in preconditioning and triggering pure IODs. Section 6 gives main conclusions and discussion.

2. Data and method

2.1) Experimental setup

Two global simulations are run using the SINTEX-F2 model (Masson et al. 2012) with the ECHAM5.3 atmosphere (Roeckner et al. 2003) at T106 spectral resolution (~1.125° x 1.125°) and 31 hybrid sigma-pressure levels, and the NEMO ocean (Madec 2008) at 0.5° x 0.5° horizontal resolution, 31 vertical levels and with the LIM2 ice model (Timmermann et al. 2005). The two model components are coupled using the Ocean–Atmosphere–Sea–Ice–Soil (OASIS3) coupler (Valcke 2006). The coupling information is exchanged every 2h. The model does not require flux adjustment to maintain a near stable climate, and accurately simulates the tropical Pacific SST mean state, ENSO variability, and the monsoon–IOD–ENSO relationships (Masson et al. 2012; Terray et al. 2012, 2016; Crétat et al. 2016). It is also a state-of-the-art tool to forecast tropical variability (Doi et al. 2016).

A 210-yr fully coupled ocean-atmosphere simulation is used as a control (CTL hereafter). The CTL is compared to a 110-yr partially coupled simulation similar to CTL, except over the tropical Pacific (30°S–30°N band, see Fig. 1h in Crétat et al. 2016) where SST is nudged toward the CTL daily climatology. This partially coupled simulation will be called FTPC here and after. Following Luo et al. (2005), the nudging method used in the FTPC modifies the non-solar heat fluxes in the tropical Pacific Ocean through a correction term, scaling with the SST model error, that completely removes ENSO-scale variability without affecting the physical consistency between SST and ocean dynamics in the nudged domain (Prodhomme et al. 2015; Terray et al. 2016). The damping term in this nudging technique (-2400 W m^{-2} K^{-1})

corresponds to the 1-day relaxation time for temperature in a 50-m ocean layer. The first 10 years of both simulations are excluded to let the model spin-ups.

2.2) Observations and reanalyses

Multiple data sources are used for model validation. SST are taken from the 1° x 1° Hadley Centre Sea Ice and Sea Surface Temperature dataset V1.1 (HadISST; Rayner et al. 2003) available from 1870 onwards. The depth of the 20°C isotherm (20D) is used as a proxy for thermocline depth and is computed using the ocean temperature profiles from the SODA V2.2.4 reanalysis (Giese and Ray 2011), available for 1871–2008 at the 0.5° x 0.5° horizontal resolution and 40 vertical levels. The SODA V2.2.4 wind stress, which is derived from the NOAA 20th Century Reanalysis (Compo et al. 2011), is also used for estimating the Bjerknes feedback associated with IOD during its peak season in Section 3.2. Since SODA produces its own SST physically consistent with the 20D and wind stress time series used here, this alternate SST dataset has been used to assess the robustness of the strength in the observed Bjerknes feedback in Section 2.3. However, this different SST dataset show similar results, so we only present here the results with HadISST SST in this study. Large-scale atmospheric circulation, including 10-m and 850-hPa winds and 200-hPa velocity potential, is provided by the 1.5° x 1.5° ECMWF ERA-Interim reanalysis (ERA-I; Dee et al. 2011) available from 1979 onwards. All these quantities are interpolated onto the model resolution to foster direct comparison with the CTL and FTPC and analyzed for the 1979–2008 period since ERA-I starts in 1979 and SODA data ends in 2008.

2.3) Methods

The IOD index is first defined as the SST anomaly gradient between the western equatorial

IO (50°–70°E, 10°S–10°N) and the southeastern equatorial IO (90°–110°E, 10°S–Eq) following Saji et al. (1999), and is used as a baseline for discussing a refined Bjerknes feedback definition of the IOD based on a multivariate technique accounting for the IOD pattern distortion in current coupled models (Cai and Cowan 2013; Terray et al. 2012; Crétat et al. 2016).

The strength of the Bjerknes feedback is defined using a singular value decomposition technique (Wallace et al. 1990; Bretherton et al. 1992) applied to the covariance matrix between all couplets of SST, 20D and wind stress (USTR) monthly anomalies in the 10°S–10°N band during boreal fall (i.e., SON). This approach, called Maximum Covariance Analysis (MCA), has been demonstrated to be more efficient than simple regression method based on area-averaged time series for studying the Bjerknes feedback in the tropical Pacific (Masson et al. 2012; Terray et al. 2016). The MCA between two fields extracts modes of spatio-temporal co-variability ranked according to their square covariance fraction (SCF). For each mode, each field is characterized by an expansion coefficient (EC) time series and an associated spatial pattern. The regression map between one field and its EC time series, the so-called "homogenous vector", gives its spatial pattern. The first mode of the three MCAs (between each pair of variables in the set of SST, 20D and wind stress) only is analyzed here because it documents each branch of the IOD-related Bjerknes feedback and explains most of the co-variability between the different couplets in both observations and simulations. The strength of this feedback is assessed using the correlation value (r) between the EC time series of the two fields and the normalized root-mean-square covariance (NC; Zhang et al. 1998) measuring how strongly related the coupled patterns are. The relationship between the Bjerknes feedback and IOD is also assessed by correlating each EC time series to the Saji's IOD index to test the robustness of our approach.

The IOD precursors and their associated mechanisms are finally examined through regression analyses. The statistical confidence of these regressions is evaluated by comparing the slope of each regression to the 90^{th} percentile threshold value derived from 1000 regressions with randomly permuted regressor having mean and variance similar to the original regressor.

3. Effects of ENSO on boreal fall IOD patterns and associated Bjerknes feedback

This section evaluates the model ability in simulating boreal fall IOD pattern/amplitude and associated Bjerknes feedback and assesses the extent to which these characteristics are influenced by ENSO.

3.1 Boreal fall IOD pattern and amplitude

The standard deviations of the Saji's IOD index during SON are 0.39, 0.48, and 0.35 K for the observations and the CTL and FTPC experiments, respectively. This suggests IOD does still exist without ENSO as an intrinsic mode of variability, but with slight reduction in amplitude, consistent with previous studies (Fischer et al. 2005; Behera et al. 2006; Luo et al. 2010; Santoso et al. 2012; Sun et al. 2015; Wang et al. 2016; Crétat at al. 2016). The observed seasonal phase-locking of IOD is also well reproduced by the CTL and FTPC experiments (not shown; see Crétat et al. 2016). The regression maps of the climate anomalies related to the IOD during its peak season (e.g., boreal fall) are shown in Fig. 1. In the observations, pIODs oppose cool SST, shallow thermocline and below-than-normal rainfall anomalies in the eastern equatorial IO to reversed anomalies further west and these equatorial SST and rainfall gradients are well correlated to the equatorial easterly zonal wind anomalies over the

central IO (Fig. 1a-b). The SST and 20D anomalous patterns are more tightly coupled in the eastern equatorial than western tropical IO, consistent with previous studies (Xie et al. 2002; Schott et al. 2009).

The IOD pattern is very similar between the two experiments and captures the main observed features (Fig. 1c-f). The two experiments largely overestimate the spatial coverage of cool SST and negative 20D anomalies in the eastern IO, especially along the equator (Fig. 1c-d) due to exaggerated boreal fall upwelling in the SINTEX and other models (Fischer et al. 2005; Cai et al. 2009; Liu et al 2014). Also, SST warming and its coupling with rainfall are underestimated over the western and southwestern IO regions where the simulated thermocline is too deep all year long (not shown). These common errors suggest that a large part of the model IOD biases may have a local origin internal to the IO or, at least, that these errors are not linked to deficiencies in the simulation of ENSO in our coupled model.

3.2 IOD and Bjerknes feedback

The Bjerknes feedback is examined during the IOD peak season based on the summary statistics for the first mode of the three MCAs (see Section 2.3), shown in Tables 1-3, and the homogeneous maps (Fig. 2). These three MCA1s account for most of the SST–20D, SST–USTR and 20D–USTR co-variability during SON in both the observations and the model, with SFC ranging from 79% up to 97% depending on both the couplet and data considered (Tables 1-3; column 1). Furthermore, the EC time series and homogeneous maps of SST derived from both the SST–20D and SST–USTR couplets are similar, with temporal and spatial correlations above +0.99 for both the observations and the simulations (not shown). This is why the SST variance described by MCA1 is almost equal in the SST–USTR and

SST–20D couplets (Tables 1-2; column 4). Such similarity also stands for 20D (Tables 2-3; columns 4-5, respectively) and USTR (Tables 1,3; column 5). Therefore, the three MCA1s depict different facets of a unique ocean-atmosphere coupled mode of co-variability, the Bjerknes feedback, which explains most of the ocean-atmosphere co-variability during boreal fall. The patterns of this coupled mode (Fig. 2) clearly resemble the Saji's IOD patterns (Fig. 1), with east-west asymmetry in SST and 20D in the equatorial IO (Fig. 2a-f) coupled to strong easterly USTR anomalies over the central tropical IO (Fig. 2g-i). However, the USTR anomalous pattern is symmetrical about the equator in the two simulations and resembles to a Gill-type atmospheric response to convection anomalies over the eastern equatorial IO and Maritime Continent (Schott et al. 2009). On the other hand, the observed SST and USTR patterns are much more asymmetrical. This suggests that observed SST variability over the southeast IO modulates atmospheric convection and drives a strong asymmetrical atmospheric Rossby wave response to its west (Li et al. 2003). Despite these differences, the eastern IO dominates the co-variability between SST, USTR and 20D during SON in both observations and simulations. The year-to-year variability of this coupled mode is also phased to that of the Saji's IOD definition since the latter is highly and positively correlated with the different EC time series (Tables 1-3; columns 6-7, respectively). Thus, variability of the EC time series explains well the amplitude of the IOD as viewed from the strength of the Bjerknes feedback.

This confirms the key-role of the positive Bjerknes feedback during the mature phase of observed and simulated IODs (e.g., Li et al. 2003; Fischer et al. 2005; Spencer et al. 2005; Schott et al. 2009). Some differences are, however, noticeable between the observations and the model. Despite exaggerated IOD amplitude in the model, the correlations between the Saji's IOD index and the EC time series are systematically greater in the observations, especially for the different 20D EC time series (Tables 2-3; column 6). This difference is

fairly reduced when removing the 5°S–5°N band in the western IO box prior to compute the Saji's IOD index in the model (column 7 in Tables 1-3). The use of the Bjerknes-oriented IOD definition allows taking into account such pattern distortion in the model (Fig. 1) and illustrates the benefits of our MCA approach.

The strength of the Bjerknes feedback may be quantified by the SFC, NC and r statistics in each MCA (see Section 2.3). The SFC, NC and r values between the EC time series of the left and right fields are strong whatever the couplet and data considered (Tables 1-3; columns 1-3, respectively). However, some differences are again noticeable between the observations and the model. First, the hierarchy in the coupling strength is metric dependent in the observations, while robust across the different metrics in the model, with the SST–20D and SST–USTR couplings systematically ranked first and last, respectively. The model also exaggerates the strength of the SST–20D and USTR–20D couplings, even in the absence of ENSO. Once again, this model bias relates to too shallow thermocline over the eastern equatorial IO (not shown) that exacerbates both the thermocline response to the wind forcing and the SST response to the thermocline forcing (Figs. 1c,e and 2b-c).

Removing ENSO slightly but significantly weakens the IOD-related Bjerknes feedback, as reflected by systematic lower statistical scores for the FTPC than the CTL (Tables 1-3; columns 1-3, respectively). While a large fraction of the positive Bjerknes feedback is linked to ocean-atmosphere interaction internal to the IO, in accordance with Fischer et al. (2005) and Behera et al. (2006), this feedback is amplified by ENSO. The main difference concerns the SST–USTR coupling, which is about 15% greater in the presence of ENSO according to the SFC metric (Table 1; column 1). Interestingly, the amplification of this coupling by ENSO is associated with increased SST variance accounted for by MCA1, while USTR variance

remains similar between the two simulations. This means that the equatorial IO SST response to similar variation in wind stress is stronger in the presence than absence of ENSO. Despite similar USTR variance accounted for by SST–USTR MCA1, USTR anomalies are greater along the central equatorial IO in the presence of ENSO (Figs. 2h,i). This suggests that ENSO may modify the IOD-related eastward Sea Level Pressure (SLP) gradient through atmospheric bridge (e.g., Hastenrath 2000) favoring easterly/westerly wind anomalies during boreal fall of developing El Niño/La Niña events (Hastenrath and Polzin 2004), hence boosting the local SST–USTR and SST–20D coupling strength.

In summary, the model suffers from classical biases found in most state-of-the-art coupled models that lead to imperfect representation of the IOD and a stronger positive Bjerknes feedback during boreal fall (Liu et al. 2014). Second, the IOD-related Bjerknes feedback is amplified by ENSO in our modeling framework, especially the surface wind–SST coupling, which can be attributed to the strong control of ENSO through the Indo-Pacific Walker circulation on the eastward SLP gradient along the equatorial IO during boreal fall.

4. Looking for IOD precursors

We now seek for identifying the IOD precursors in the observations and the experiments. Figures 3 and 4 show the non-standardized SST EC time series averaged in SON(0) regressed onto standardized anomalies of ocean thermal state (SST and 20D) and atmospheric circulation (850-hPa wind and 200-hPa velocity potential) from SON(0) back to the preceding boreal winter (DJF(0)). The choice of the IOD index (i.e., Saji's SST or ECs from the different MCA1s) to be regressed does not affect the results. Here, the IOD prediction patterns are expressed in °C for one standard deviation of each local (i.e., at each grid-point)

363 regressor variable to foster direct comparisons between the different seasons, datasets and
364 parameters analyzed.
365
366 4.1 ENSO
367
368 In both observations and CTL, ENSO is one of the main precursors for IOD during late spring
369 and boreal summer since the Pacific SST, the east-west asymmetry of the equatorial Pacific
370 heat content in MAM(0) and JJA(0) (Fig. 3b-c,f-g) and the low-level wind anomalies over the
371 Western North Pacific in MAM(0) (Fig. 4c,g) appear to be good precursors for IOD at these
372 short-time leads. This is consistent with the literature (Annamalai et al. 2003; Li et al. 2003;
373 Gualdi et al. 2003; Bracco et al. 2005; Fischer et al. 2005; Behera et al. 2006). Interestingly,
374 the IOD predictions by the 200-hPa velocity potential fields over the Indo-Pacific region
375 equal to or even outperform the IOD predictions from the tropical Pacific SST at these short
376 time leads. This highlights once again the key-role of ENSO atmospheric teleconnections for
377 boosting the Bjerknes feedback over the IO.
378
379 Significant long-lead (e.g., at 10-12 months time lead) IOD predictions can be traced back to
380 well-known ENSO predictors overcoming the spring predictability barrier in both
381 observations and the CTL (Boschat et al. 2013). In DJF(0), this includes the heat content over
382 the western and central Pacific (Fig. 3d,h) that plays a key-role in the ENSO's recharge
383 oscillator paradigm (Jin et al. 1997; Meinen and McPhaden 2000), and, for CTL only, the
384 low-level zonal wind over the West Pacific (Fig. 4h), whose westerly anomalies may trigger
385 oceanic Kelvin waves propagating into the eastern equatorial Pacific. These results moderate
386 the idea that IOD may help predicting ENSO one year before its peak as an independent
387 precursor (e.g., Izumo et al. 2010; Jourdain et al. 2016) and suggest rather a biennial

predictive relationship between IOD and ENSO (Webster and Hoyos 2010). Recently, Stuecker et al. (2015, 2017) argue that IOD predictability is solely determined by ENSO predictability and ENSO signal-to-noise ratio and that the full Tropospheric Biennial Oscillation (TBO; Meehl et al. 2002, 2003) can be fully explained by ENSO dynamics and teleconnections. At first sight, our results are not contradictory with this hypothesis, but the determination of the intrinsic IOD timescale in the FTPC simulation will provide another interpretation in the next section.

Compared to the observations and the CTL, the IOD prediction patterns simulated over the Pacific in the absence of ENSO (Fig. 4i-l) are poorly significant. This underlines the poor skill of internal noise-related atmospheric variability over the Pacific for IOD prediction.

4.2 IO tropical-extratropical interactions

The pIOD prediction patterns of SST (and SLP: not shown) in DJF(0) suggest an active role of the South IO for triggering IOD (Terray and Dominiak 2005; Fischer at al. 2005; Terray et al. 2007; Zhao et al. 2009) with an atmospheric blocking over the extratropical IO that forces a southwest-northeast SST dipole between the southwestern IO, south of Madagascar, and off Australia (Fig. 3d,h). This pattern resembles the SIOD pattern (Behera and Yamagata 2001) and is well captured by the CTL, despite too zonal (Fig. 3h). The mutual predictive relationships between the IOD and SIOD are not discussed thoroughly in the literature to the best of our knowledge and are almost impossible to untangle from observations and fully coupled simulations because both modes are partly forced by ENSO (Schott et al. 2009; Terray 2011). Despite weaker amplitude, this observed SIOD pattern is also well simulated in DJF(0) by FTPC (Fig. 3l), suggesting its validity for IOD triggering even without ENSO. This

is further examined in Section 5.4.

4.3 Tropical IO waves

A last important long-range precursor for IOD relates to tropical IO oceanic waves (Fig. 3). The IOD prediction pattern derived from 20D anomalies confirms that local oceanic processes are important for IOD (e.g., Webster et al. 1999; Rao et al. 2002; Feng and Meyers 2003). Under ENSO's influence, the observed and simulated IOD prediction patterns from 20D are rather noisy spatially at long time leads (e.g., in DJF(0)), with no evident zonal dipole in the subsurface or significant IOD predictions, especially in the CTL experiment (Fig. 3d,h). This contrasts with the FTPC that displays a strong zonal dipole in DJF(0) (Fig. 3l) that rapidly reverses in sign afterwards, suggesting much biennial IOD variability simulated in the absence of ENSO (Feng and Meyers 2003; Behera et al. 2006), a point at odd with the results of Stuecker et al. (2017) and further discussed in Section 5.

In summary, the analysis highlights three potential long-range predictors for IOD: ENSO, IO tropical-extratropical interactions that exist without ENSO but are amplified by ENSO, and the role of tropical IO waves, which are damped or even masked in the presence of ENSO. Section 5 seeks for better understanding the influence of these intrinsic IO precursors and timescale without ENSO, as well as their mutual interactions by focusing mostly on the FTPC experiment.

5. IOD timescale in the absence of ENSO

5.1 IOD timescale

438

439 We first assess the intrinsic timescale (if any) of IOD variability independently of ENSO.
440 This is done by comparing auto and cross-correlations of the various EC time series between
441 the observations and the two experiments (Fig. 5; the corresponding homogenous patterns are
442 displayed in Fig. 2).

443

444 Despite ENSO and IOD are significant precursors of each other at one year lead (see Section
445 4), IOD variability is much more biennial in the absence than presence of ENSO, especially in
446 the subsurface, as demonstrated by the shape of the FTPC auto-correlations of the EC time
447 series (Fig. 5b-c). Interestingly, this biennial rhythm is also seen in the observations (Fig. 5a).
448 The lead-lag correlation analyses between the various EC time series in FTPC (Fig. 5d)
449 confirm this biennial rhythm of the ocean-atmosphere coupling sustained by the subsurface
450 when ENSO is decoupled. These results suggest that the IO is able to sustain a self-contained
451 biennial oscillation, which is at odd with Stuecker et al. (2015, 2017), but consistent with
452 older studies suggesting that IO variability in heat content and ocean dynamics may play a
453 key-role for explaining the reversal in the sign of atmospheric and SST anomalies from one
454 year to another (Feng and Meyers 2003) and sustaining the TBO (Meehl et al. 2002, 2003)
455 independently of ENSO. This IOD–TBO linkage is also consistent with several previous
456 coupled modeling studies, which demonstrate that IOD variability is more biennial when the
457 Pacific is decoupled (Fischer et al. 2005; Behera et al. 2006).

458

459 The biennial rhythm in the FTPC experiment is further assessed by regressing FTPC-climate
460 anomalies in a two-year window onto the 20D standardized SON(0) EC time series derived
461 from the SST–20D MCA1. Main results are few sensitive to the choice of the EC time series
462 considered. Figs. 6 and 7 show regression maps of monthly wind stress, SST and 20D

anomalies from Sep(-1) to Nov(0) and from Dec(0) to Nov(+1), respectively. They first confirm the biennial rhythm of the IOD with westerly USTR anomalies along the equator during boreal fall of years (-1) and (+1) coupled to thermocline deepening and SST warming in the eastern equatorial IO (Figs. 6a-c and 7j-l), and reversely during boreal fall of year 0 (Fig. 6m-o). The IOD biennial rhythm is, however, much well defined in the eastern IO than in its western part, as reflected by the rather weak and poorly significant SST and subsurface anomalies in the latter during boreal fall of years (-1) and (+1) (Figs. 6a-c and 7j-l). Complementary lead/lag composites highlight also that this biennial rhythm is more sustained by nIOD-to-pIOD than pIOD-to-nIOD transitions (not shown).

5.2 Role of oceanic waves in the biennial rhythm of IOD

Figs. 6 and 7 also suggest the importance of both equatorial and off-equatorial oceanic waves for explaining the evolution of the climate anomalies during the two-year window. During boreal fall of year (-1), westerly USTR anomalies along the equator force a fast equatorially-trapped downwelling Kelvin wave that hits Java-Sumatra, deepens the eastern equatorial IO thermocline and warms the central and eastern IO, especially between the equator and 5°S during (Fig. 6b-c). The near-equatorial westerly USTR anomalies relax in early boreal winter and remain weak until mid-spring (Fig. 6d-h). This co-occurs with the reflection of the downwelling Kelvin wave at the eastern boundary into (i) coastal Kelvin waves radiating poleward in both Hemispheres and (ii) near-equatorial downwelling Rossby waves at 3°S and ~3°N (off Java) that both contribute to deepen the thermocline in the eastern tropical IO by Dec(-1) (Fig. 6d). While the downwelling Rossby rapidly weakens at 3°S, it slowly propagates westward until early boreal spring at ~3°N and contributes to damp the negative thermocline anomalies in the Arabian Sea (Fig. 6e-h). Such evolution is reversed from Nov(0)

488 to Apr(+1) (Figs. 6o and 7a-e), consistent with a biennial rhythm.

489

490 Off-equatorial Rossby waves and their westward propagation are also clearly seen in the two-
491 year-window analyzed here (Figs. 6 and 7). Pure pIODs and their associated cold SST
492 anomalies in the eastern IO initiate in Apr-Jun(0) by an anomalous upwelling along the Java-
493 Sumatra coast (Fig. 6i-j). Note that negative 20D anomalies already exist in the eastern
494 equatorial IO during the previous months, providing a favorable preconditioning for pIOD
495 triggering, but are decoupled from the surface before May(0) (Fig. 6f-i). The SST cooling is
496 also coupled with a vigorous anomalous anticyclonic circulation over the southeastern IO
497 during Apr-Jun(0) (Fig. 6h-i). This generates a patch of downwelling pumping over the
498 eastern off-equatorial IO that favors Rossby wave development. The latter slowly propagates
499 westward during the following months, leading to thermocline deepening and SST warming
500 in the western IO (Figs. 6i-o and 7a-c), consistent with previous studies (Rao et al. 2002; Yu
501 et al. 2005; Schott et al. 2009). While these Rossby waves play a pivotal role for shoaling the
502 thermocline in the western tropical IO in boreal fall (Fig. 6m-o), the SST response remains
503 weak there. This relates once again to too deep thermocline simulated on average by the
504 SINTEX model there, even without ENSO. This may explain why the biennial rhythm is less
505 obvious in the SST EC time series (Fig. 5c). This evolution tends finally to be reversed during
506 years (-1) and (+1), but is much less significant (Figs. 6a-c and 7e-l).

507

508 However, the role of these different Rossby waves in reversing the sign of the subsurface
509 anomalies from one year to the next is unclear in the FTPC. Once they have reached the
510 western boundary, the off-equatorial Rossby waves produce persisting 20D anomalies in the
511 western IO during boreal fall and winter (Figs. 6-7) but do not reach the equatorial guide nor
512 propagate eastward along the equator. Thus, they do not seem to help IOD termination during

boreal winter, as hypothesized by Feng and Meyers (2003). Similarly, the equatorial Rossby waves do not appear to provide a significant delayed negative feedback to terminate IODs because they dissipate quickly before reaching the western IO boundary and are not reflected as packets of Kelvin waves into the equatorial wave-guide (Figs. 6-7). This also contradicts their suggested key-role in the TBO (Meehl et al. 2003).

On the other hand, thermocline anomalies between boreal fall and winter appear to be key for IOD transition and explaining changes in the sign of the biennial anomalies. As described above, an equatorially trapped upwelling/downwelling Kelvin wave partly reflects into near-equatorial upwelling/downwelling Rossby waves at the eastern IO boundary during the fall–winter transition succeeding pIOD/nIOD and preceding nIOD/pIOD events, consistent to the oceanic wave reflection theory (Yuan and Liu 2009; Wang and Yuan 2015). This is followed by a sudden inversion in the sign of thermocline anomalies along Java-Sumatra (Fig. 7c-e). The regression of 5-day 20D anomalies along the equator from Sep(-1) to Jun(0) onto monthly 20D anomalies area-averaged in the eastern equatorial IO (sea points within the box shown in Fig. 7b) during Jan(0) (Fig. 8a) confirms the persistence of the eastern equatorial IO 20D anomalies after boreal fall and their sudden change in sign during Feb(0). Once the thermocline is reversed in the eastern equatorial IO, the deepening (or shoaling) persists until boreal spring, providing very favorable conditions for nIOD (or pIOD) triggering (Figs. 6-8). The same analysis done using 20D anomalies in Feb(0) as regressor (Fig. 8b) allows focusing on the potential cause of the 20D anomaly reversal during the fall–winter transition. Results demonstrate that these upwelling/downwelling anomalies in Feb(0) are not related to the reflection of the upwelling/downwelling Kelvin wave at the eastern IO boundary. They can be traced back to upwelling/downwelling favorable 20D anomalies in the western IO that propagate eastward and cross the basin in about 20-40 days. This intraseasonal propagating

signal is decoupled to monthly USTR anomalies over the eastern equatorial IO during boreal winter, but it may relate to their relaxation over the western and central equatorial IO at this time (Figs. 6e-f and 7b-c) and/or be forced by equatorial westerly wind anomalies at the intraseasonal timescale (Han and Shinoda 2005; Schott et al. 2009).

5.3 Role of intraseasonal disturbances in the reversal of biennial oceanic and atmospheric anomalies in the IO

Intraseasonal variability over the equatorial IO from November to February has been suggested as an important factor in the termination of IODs both in observations and simulations (Rao and Yamagata 2004; Han et al. 2006; Rao et al. 2007, 2009). Here, we assess the importance of this factor on the reversal of the biennial IO anomalies when ENSO variability is removed by regressing the fall-to-spring evolution of near-equatorial 5-day outgoing longwave radiation (OLR) and USTR anomalies over the IO onto monthly 20D anomalies area-averaged in the eastern equatorial IO (box in Fig. 7b) during both January and February (Fig. 8c-f). The 20D variability in the eastern equatorial IO is significantly associated with eastward propagating convective disturbances, especially for the February 20D anomalies (Fig. 8c-d). These successive intraseasonal convective disturbances are triggered in the western or central IO and reach the eastern IO in about 30 days. This 20–40-day signal is faster than the observed 30–60-day MJO (Han and Shinoda 2005; Schott et al. 2009), but is consistent with results obtained with an older version of the SINTEX model (Rao et al. 2007). The associated intraseasonal USTR anomalies may excite equatorial upwelling/downwelling Kelvin waves (Schott et al. 2009) responsible for the shoaling/deepening of the thermocline in the eastern IO in February (Fig. 8b,d,f). This suggests that the MJO is a major contributor to both the termination of IODs and the reversal

563 of the biennial climate anomalies in the absence of ENSO (Han et al. 2006; Rao et al. 2007,
564 2009).
565
566 To further confirm the potential role of the MJO in driven the thermocline reversal occurring
567 between December and February (Figs. 6d-f and 7a-c) in the FTPC, we computed linear
568 correlations at the pentad timescale between 20D anomalies area-averaged in the eastern
569 equatorial IO to zonal anomalies in 20D, OLR and USTR averaged in the 2°S–2°N band. The
570 20D index (box in Fig. 7b) covers a fixed period of 13 pentads centered onto Dec 15, while
571 zonal anomalies cover a sliding period of 13 pentads from 12 pentads prior to 12 pentads after
572 Dec 15. The correlations are performed for each year without any band-pass filtering and are
573 then averaged either over the entire period or for years following pIODs and nIODs. The
574 results (Fig. 9) are very robust since they do not depend on the centering date selected
575 between December 1 and February 1 nor on the choice of the EC time series used to extract
576 IOD events (not shown). They do show propagation of equatorial thermocline anomalies,
577 consistent with Fig. 8b, and a thermocline reversal in the eastern equatorial IO between boreal
578 fall and winter (Fig. 9a-c). This reversal is clearly favored by the MJO, as reflected by
579 positive (negative) correlations with USTR at negative (positive) lags (Fig. 9d-f) and negative
580 correlations with OLR propagating eastward from the western IO to the eastern IO from lag -
581 4 to lag +4. The role of the MJO in the thermocline reversal seems stronger during nIOD-to-
582 pIOD transitions (Fig. 9c,f,i), which exhibit clearer eastward propagating signals than during
583 pIOD-to-nIOD transitions (Fig. 9b,e,h). On the other hand, the IOD variability also modulates
584 the strength of the intraseasonal activity, with nIODs enhancing the MJO in the following
585 boreal winter, consistent with Shinoda and Han (2005).
586
587 5.4 Role of tropical-extratropical IO interactions in IOD triggering

The subsurface dynamics play a pivotal role for preconditioning IODs and sustaining their biennial rhythm, but are not sufficient for triggering them. This is illustrated in Fig. 10, which shows the monthly evolution of 20D anomalies in the eastern equatorial IO (box in Fig. 7b) before and after pIODs and nIODs in FTPC. This is also consistent with Fig. 6g-j, which shows that pure pIODs/nIODs are triggered by coupled cold/warm SST and anticyclonic/cyclonic circulation anomalies over the southeast IO originating from the extratropical IO.

The role of such tropical-extratropical IO interactions in triggering pure IODs is further examined with regression maps of quarterly atmospheric and oceanic anomalies from SON(-1) to SON(0) over the tropical-extratropical belt (Figs 11-12). In SON(-1), the abnormally active convection over the eastern equatorial IO associated with nIODs favors local upper-level divergence and shifts westward the Indo-Pacific Walker circulation (Fig. 11a). The upper-level anomalous dipole in velocity potential persists and slowly moves eastward in DJF(0) (Fig. 11a-b), similar to what is observed during ENSO (Lau et Nath, 2000, 2003). The associated convection and diabatic heating anomalies force a Gill-type response immediately westward of them with two low-level cyclonic cells at both sides of the equator and equatorial westerly anomalies. They also excite an atmospheric Rossby wave-train over South IO from SON(-1) to JJA(0) and the associated mid-latitude anomalous SLP pattern slowly propagates eastward in response to the eastward propagation of the diabatic heating anomalies in the tropics (Fig. 11a-d). This suggests that tropical convection over the IO is an important driver for mid-latitude circulation (Cai et al. 2011), with nIOD conditions in SON(-1) strengthening subtropical anticyclones during DJF(0) and associated blocking over the South IO. This atmospheric teleconnection between the tropical and extra-tropical IO in the absence of

ENSO generates thus a strong co-variability between boreal fall nIODs and boreal winter positive SIOD events (Fig. 12b,c; Behera and Yamagata 2001), consistent with the fact that SIODs are mainly forced by pulsations of the Mascarene High (Terray 2011; Morioka et al. 2012).

In MAM(0), the SIOD pattern in SST persists and its cold SST anomalies over the southeast IO (Fig. 12c) force a baroclinic circulation over the southeast IO (between Equator and 30°S) with an anomalous 850-hPa anticyclone coupled to anomalous 200-hPa convergence (Fig. 11c). These coupled ocean-atmosphere anomalies move northeastward during boreal spring and early summer (Fig. 6g-j), consistent with previous studies (Terray et al. 2007). This significantly affects tropical convection by pushing equatorial convection from the eastern IO to the Maritime Continent and surrounding Western Pacific during MAM(0). These coupled anomalies play also a key-role for triggering IODs after the preconditioning of the subsurface, as discussed in Section 5.2. The low-level anticyclonic anomaly favors easterly wind anomalies along the equator in May(0) (Fig. 6i), which trigger an upwelling Kelvin wave and weaken the Wirtki jet during boreal spring and early summer (Fig. 6i-j). This induces a fast thermocline shoaling over the whole eastern equatorial IO and initiates a positive Bjerknes feedback during Jun(0), promoting the persistence of the eastward equatorial low-level wind and thermocline anomalies there during the following months (Fig. 6i-o). These complex but robust interactions between the tropical and subtropical IO across the seasons are sufficiently strong to impose a well-defined biennial rhythm to IOD variability in the FTPC (Fig. 12).

6. Conclusion and discussion

This study seeks for examining and understanding the intrinsic IOD precursors and timescale

638 in the absence of ENSO. This is achieved by analyzing a partially decoupled ocean-
639 atmosphere experiment (FTPC) with ENSO variability removed in the tropical Pacific. The
640 FTPC experiment is compared to a fully coupled control (CTL) and observations to
641 disentangle local and remote model biases and the effects of ENSO on IOD, its precursors and
642 timescale.
643
644 First, the IOD does still exist without ENSO as an intrinsic mode of variability, but with
645 reduced amplitude (Figs. 1-2). This is consistent with many previous studies (Fischer et al.
646 2005; Behera et al. 2006; Luo et al. 2010; Santoso et al. 2012; Sun et al. 2015; Wang et al.
647 2016; Crétat at al. 2016). Pure IODs have about similar patterns with and without ENSO,
648 indicating IODs take their root within the IO in our modeling framework. Main differences
649 between the two experiments concern a weakened Bjerknes feedback in the absence of
650 ENSO, especially the SST–USTR coupling that is about 15% weaker (Fig. 2 and Table 1).
651 Our results show that ENSO amplifies the IOD-related Bjerknes feedback by modifying the
652 eastward SLP gradient and the associated zonal wind anomalies over the equatorial IO
653 through the atmospheric bridge (e.g., Hastenrath 2000; Hastenrath and Polzin 2004). More
654 importantly, the IOD timescale greatly differs between the two experiments (Fig. 5). IOD
655 timescale appears to be much more biennial in the absence of ENSO, in line with Feng and
656 Meyers (2003) and Behera et al. (2006). This IOD biennial rhythm is much clearer in the
657 subsurface than at the surface and in the eastern than the western IO (Figs. 6-7). This biennial
658 rhythm is also found for the recent observations, consistent with Meehl et al. (2002, 2003) and
659 Webster and Hoyos (2010), but surprisingly not in our 200-yr long CTL. This differs from
660 Stuecker et al. (2017) who argue that IOD biennial timescale can be fully explained by
661 ENSO. The reasons of this difference are not due to improper simulated ENSO periodicity
662 that is fairly well captured by the CTL (Masson et al. 2012; Terray et al. 2016). The

hypothesis that the IOD timescale and TBO may be solely explained by ENSO dynamics (Stuecker et al. 2015, 2017) is thus not consistent with our modeling results since the experiment with ENSO does not simulate biennial IOD timescale, while the experiment without ENSO does.

Despite IOD has its own timescale, ENSO appears as one of the main short- and long-time lead precursors for IOD in the observations and the CTL, confirming the CTL accurately simulates ENSO influence on IOD. Apart from ENSO, two long-time IOD precursors are found within the IO. The first involves tropical-extratropical interactions linking the IOD and the SIOD (Behera and Yamagata 2001) that exist without ENSO but are amplified by ENSO. The second involves the subsurface and Kelvin waves in the equatorial IO. This oceanic precursor, which is intimately associated with the IOD biennial timescale, is damped or even masked in the presence of ENSO because of the influence of the associated Walker circulation anomalies on the equatorial IO zonal wind (Hastenrath and Polzin 2004). A detailed analysis points toward a complementary role between equatorial subsurface dynamics and tropical-extratropical interactions in preconditioning and triggering IOD events, respectively, and in sustaining the biennial oscillation over the IO when ENSO is decoupled. In our modeling framework, reflections of equatorial and off-equatorial oceanic waves on the western and eastern IO boundaries cannot explain the IOD biennial timescale, contrary to previous hypotheses (Feng and Meyers 2003; Meehl et al. 2002, 2003).

Our results suggest that the rapid reversal of the thermocline anomalies during the decaying phase of pure IODs (i.e., during December–February in the FTPC experiment) is key for preconditioning subsequent IOD development of opposite sign the next year. This sudden reversal relates to intraseasonal disturbances reminiscent of the MJO during boreal winter

following IOD events, especially after negative IOD events. This complements the influence of the MJO on IOD termination reported in both observations and simulations (Rao and Yamagata 2004; Han et al. 2006; Rao et al. 2007, 2009) by showing that MJO and IOD are tightly interconnected. Such coupling between the MJO and the IO subsurface is, however, not sufficient for triggering pure IODs (Fig. 10).

Such triggering originates from the extratropical IO (Figs. 6-7 and 11-12), consistent with several previous studies (Terray and Dominiak 2005; Fischer at al. 2005; Terray et al. 2007; Zhao et al. 2009). Here, we show complex two-way interactions between IOD and SIOD. First, IOD-related convection forces the mid-latitude circulation (Cai et al. 2011; Morioka et al. 2012), with nIOD conditions strengthening the South IO anticyclone and associated blocking during boreal winter, hence promoting positive SIOD events. Second, this blocking and associated cold SST anomalies over the southeast IO persist until the subsequent boreal spring and force an anomalous anticyclonic circulation at the surface over the southeast IO. Such coupled ocean-atmosphere anomalies over the southeast IO are fundamental for triggering IODs during boreal spring after the preconditioning of the subsurface in boreal winter. The reverse prevails for pIOD conditions.

These complementary influences of equatorial IO dynamics, intraseasonal atmospheric disturbances and tropical-extratropical interactions in triggering IOD and promoting biennial variability may shed new lights for improving our ability to predict IOD and its climate impacts.

Acknowledgments

713 This work was funded by the Earth System Science Organization, Ministry of Earth Sciences,
714 Government of India under Monsoon Mission (Project No. MM/SERP/CNRS/2013/INT-
715 10/002 Contribution #MM/PASCAL/RP/07. This work was performed using HPC resources
716 from GENCI-IDRIS (Grants 2015, 2016, 2017 – 016895).
717

718 **References**

719

720 Annamalai H, R Murtugudde, J Potemra, SP Xie, P Liu, B Wang (2003) Coupled dynamics
721 over the Indian Ocean: Spring initiation of the zonal mode. Deep-Sea Res II, 50:2305–
722 2330

723 Ashok K, Z Guan, T Yamagata (2003) A look at the relationship between the ENSO and the
724 Indian Ocean dipole. J Meteor Soc Japan, 81:41–56

725 Battisti DS, AC Hirst (1989) Interannual variability in the tropical atmosphere-ocean system:
726 influences of the basic state, ocean geometry and nonlinearity. J Atmos Sci 46:1687–
727 1712

728 Behera SK, T Yamagata (2001) Subtropical SST dipole events in the southern Indian Ocean.
729 Geophys Res Lett 28:327–330

730 Behera SK, JJ Luo, S Masson, P Delecluse, S Gualdi, A Navarra, T Yamagata (2005)
731 Paramount impact of the Indian Ocean dipole on the East African short rains: A CGCM
732 study. J Clim 18:4514–4530

733 Behera SK, JJ Luo, S Masson, SA Rao, H Sakuma, T Yamagata (2006) A CGCM study on
734 the interaction between IOD and ENSO. J Clim 19:1608–1705

735 Black E, J Slingo, KR Sperber (2003) An observational study of the relationship between
736 excessively strong short rains in coastal East Africa and Indian Ocean SST. Mon Wea
737 Rev 131:74–94

738 Boschat G, P Terray, S Masson (2013) Extratropical forcing of ENSO. Geophys Res Lett
739 40:1–7

740 Bracco A, F Kucharski, F Molteni (2005) Internal and forced modes of variability in the
741 Indian Ocean. Geophys Res Lett 32, L12707, doi:10.1029/2005GL023154

742 Bretherton CS, C Smith, JM Wallace (1992) An intercomparison of methods for finding
743 coupled patterns in climate data. J Clim 5:541–560
744 Cai W, A Sullivan, T Cowan T (2009) Climate change contributes to more frequent
745 consecutive positive Indian Ocean dipole events. Geophys Res Lett 36, L23704,
746 doi:10.1029/2009GL040163
747 Cai W, P van Rensch, T Cowan, HH Hendon (2011) Teleconnection pathways of ENSO and
748 the IOD and the mechanisms for impacts on Australian rainfall. J. Climate, 24 :3910–
749 3923
750 Cai W, T Cowan (2013) Why is the amplitude of the Indian Ocean Dipole overly large in
751 CMIP3 and CMIP5 climate models?. Geophys Res Lett 40:1200-1205,
752 doi:10.1002/grl.50208
753 Chan SC, SK Behera, T Yamagata (2008) Indian Ocean Dipole influence on South American
754 rainfall. Geophys Res Lett 35:L14S12, doi:10.1029/2008GL034204
755 Compo GP, P Sardeshmukh (2010) Removing ENSO-related variations from the climate
756 records. J Clim 23:1957–1978
757 Compo GP and Coauthors (2011) The twentieth century reanalysis project. Q J R Meteorol
758 Soc 137:1–28
759 Crétat J, P Terray, S Masson, KP Sooraj, MK Roxy (2016) Indian Ocean and Indian summer
760 monsoon: relationships without ENSO in ocean-atmosphere coupled simulations. Clim
761 Dyn, online, doi:10.1007/s00382-016-3387-x
762 Dee DP and Coauthors (2011) The ERA-Interim reanalysis: configuration and performance of
763 the data assimilation system. Q J R Meteorol Soc 137:553–597
764 Delman AS, J Sprintall, JL McClean, LD Talley (2016) Anomalous Java cooling at the
765 initiation of positive Indian Ocean Dipole events. J Geophys Res Oc,
766 doi:10.1002/2016JC011635

767 Doi T, SK Behera, T Yamagata (2016) Improved seasonal prediction using the SINTEX-F2
768 coupled model. J Adv Mod Earth Syst 8:1847–1867
769 Drbohlav HKL, S Gualdi, A Navarra (2007) A diagnostic study of the Indian Ocean dipole
770 mode in El Niño and non-El Niño years. J Clim 20:2961–2977
771 Feng M, G Meyers (2003) Interannual variability in the tropical Indian Ocean: a two-year
772 time-scale of Indian Ocean Dipole. Deep-Sea Res II 50:2263–2284
773 Fischer AS, P Terray, P Delecluse, S Gualdi, E Guilyardi (2005) Two independent triggers for
774 the Indian Ocean dipole/zonal mode in a coupled GCM. J Clim 18:3428–3449
775 Gadgil S, PN Vinayachandran, PA Francis, S Gadgil (2004) Extremes of the Indian summer
776 monsoon rainfall, ENSO and equatorial Indian Ocean oscillation. Geophys Res Lett 31,
777 L12213, doi:10.1029/2004GL019733
778 Giese BS, S Ray (2011) El Niño variability in simple ocean data assimilation (SODA), 1871–
779 2008. J Geophys Res 116:C02024, doi:10.1029/2010JC006695
780 Gualdi S, E Guilyardi, A Navarra, S Masina, P Delecluse (2003) The interannual variability in
781 the tropical Indian Ocean as simulated by a CGCM. Clim Dyn 20:567–582
782 Guo F, Q Liu, XT Zheng, S Sun (2013) The role of barrier layer in Southeastern Arabian Sea
783 during the development of positive Indian Ocean Dipole events. Ocean Coast Res
784 12:245–252
785 Guo F, Q Liu, S Sun, J Yang (2015) Three types of Indian Ocean Dipoles. J Clim 28:3073–
786 3092
787 Han W, T Shinoda, LL Fu, JP McCreary (2006) Impact of atmospheric intraseasonal
788 oscillations on the Indian Ocean dipole during the 1990s. J Phys Oceanogr 111:679–690
789 Hastenrath S (2000) Zonal circulations over the equatorial Indian Ocean. J Clim 13:2746–
790 2756

791 Hastenrath S, D Polzin (2004) Dynamics of the surface wind field over the equatorial Indian
792 Ocean. Q J R Meteorol Soc 130:503-517
793 Hendon HH (2003) Indonesian rainfall variability: impact of ENSO and local air–sea
794 interaction. J Clim 16:1775–1790
795 Hong CC, T Li, YC LinHo Chen (2010) Asymmetry of the Indian Ocean basinwide SST
796 anomalies: roles of ENSO and IOD. J Clim 23:3563–3576
797 Izumo T, J Vialard, M Lengaigne, C de Boyer Montégut, SK Behera, JJ Luo, S Cravatte, S
798 Masson, T Yamagata (2010) Influence of the state of the Indian Ocean Dipole on the
799 following year's El Niño. Nature Geoscience 3:168–172
800 Jin FF (1997) An equatorial ocean recharge paradigm for ENSO. Part I: conceptual model. J
801 Atmos Sci 54:811–829
802 Jourdain NC, M Lengaigne, J Vialard, T Izumo, AS Gupta (2016) Further insights on the
803 influence of the Indian Ocean Dipole on the following year's ENSO from observations
804 and CMIP5 models. J Clim 29:637–658
805 Kajikawa Y, T Yasunari, R Kawamura (2003) The role of the local Hadley circulation over
806 the Western Pacific on the zonally asymmetric anomalies over the Indian Ocean. J
807 Meteor Soc Japan 81:259–276
808 Kajtar JB, A Santoso, MH England, W Cai (2016) Tropical climate variability: interactions
809 across the Pacific, Indian, and Atlantic Oceans. Clim Dyn, doi:10.1007/s00382-016-
810 3199-z
811 Klein SA, BJ Soden, NC Lau (1999) Remote sea surface temperature variations during
812 ENSO: evidence for a tropical atmospheric bridge. J Clim 12:917–932
813 Krishnaswamy J, S Vaidyanathan, B Rajagopalan, M Bonell, M Sankaran, RS Bhalla, S
814 Badiger (2015) Non-stationary and non-linear influence of ENSO and Indian Ocean

Dipole on the variability of Indian monsoon rainfall and extreme rain events. Clim Dyn 45:175–184

Lau NC, MJ Nath (2000) Impact of ENSO on the variability of the Asian–Australian monsoons as simulated in GCM experiments. J Clim 13:4287–4309

Lau NC, MJ Nath (2003) Atmosphere–ocean variations in the Indo-Pacific sector during ENSO episode. J Clim 16:3–20

Li T, B Wang, CP Chang, YS Zhang (2003) A theory for the Indian Ocean dipole-zonal mode. J Atmos Sci 60:2119–2135

Liu L, SP Xie, XT Zheng, T Li, Y Du, G Huang, WD Yu (2014) Indian Ocean variability in the CMIP5 multi-model ensemble: the zonal dipole mode. Clim Dyn 43:1715–1730

Liu H, Y Tang, D Chen, T Lian (2016) Predictability of the Indian Ocean Dipole in the coupled models. Clim Dyn, doi:10.1007/s00382-016-3187-3

Luo JJ, S Masson, S Behera, S Shingu, T Yamagata (2005) Seasonal climate predictability in a coupled OAGCM using a different approach for ensemble forecasts. J Clim 18 :4474–4497

Luo JJ, R Zhang, S Behera, Y Masumoto, FF Jin, R Lukas, T Yamagata (2010) Interactions between El Nino and extreme Indian Ocean dipole. J Clim 23: 726-742

Madec G (2008) NEMO ocean engine. Note du Pôle de modélisation, Institut Pierre-Simon Laplace (IPSL), France. No 27. ISSN No 1288-1619

Masson S, P Terray, G Madec, JJ Luo, T Yamagata, K Takahashi (2012) Impact of intra-daily SST variability on ENSO characteristics in a coupled model. Clim Dyn 39:681–707

McPhaden MJ (1999) Genesis and evolution of the 1997–1998 El Niño. Science 283:950–954

McPhaden MJ, M Nagura (2014) Indian Ocean dipole interpreted in terms of recharge oscillator theory. Clim Dyn 42:1569–1586

839 Meehl GA, JM Arblaster (2002) Indian monsoon GCM sensitivity experiments testing
840 tropospheric biennial oscillation transition conditions. J Clim 15:923–944
841 Meehl GA, JM Arblaster, J Loschnigg (2003) Coupled ocean–atmosphere dynamical
842 processes in the tropical Indian and Pacific Oceans and the TBO. J Clim 16:2138–2158
843 Meinen CS, MJ McPhaden (2000) Observations of warm water volume changes in the
844 equatorial Pacific and their relationship to El Niño and La Niña. J Clim 13:3551–3559
845 Morioka Y, S Masson, P Terray, JJ Luo, T Yamagata (2012) Subtropical dipole modes
846 simulated in a coupled general circulation model. J Clim 25:4029–4047
847 Murtugudde R, JP McCreary Jr, AJ Busalacchi (2000) Oceanic processes associated with
848 anomalous events in the Indian Ocean with relevance to 1997–1998. J Geophys Res
849 105:3295–3306
850 Prodhomme C, P Terray, S Masson, T Izumo, T Tozuka, T Yamagata (2014) Impacts of
851 Indian Ocean SST biases on the Indian monsoon: as simulated in a global coupled
852 model. Clim Dyn 42:271–290
853 Prodhomme C, P Terray, S Masson, G Boschat, T Izumo (2015) Oceanic factors controlling
854 the Indian summer monsoon onset in a coupled model. Clim Dyn 44:977–1002
855 Rao SA, SK Behera, Y Masumoto, T Yamagata (2002) Interannual subsurface variability in
856 the Tropical Indian Ocean with a special emphasis on the Indian Ocean Dipole. Deep-
857 Sea Res 49:1549–1572
858 Rao SA, T Yamagata (2004) Abrupt termination of Indian Ocean dipole events in response to
859 intraseasonal disturbances, Geophys Res Lett 31, L19306, doi:10.1029/2004GL020842
860 Rao SA, SK Behera (2005) Subsurface influence on SST in the tropical Indian Ocean:
861 structure and interannual variability. Dyn Atmo Oceans 39:103–135
862 Rao SA, S Masson, JJ Luo, SK Behera, T Yamagata (2007) Termination of Indian Ocean
863 Dipole events in a coupled general circulation model. J Clim 20:3018–3035

Rao SA, JJ Luo, SK Behera, T Yamagata (2009) Generation and termination of Indian Ocean dipole events in 2003, 2006 and 2007. Clim Dyn 33:751–767

Rayner NA, DE Parker, EB Horton, CK Folland, LV Alexander, DP Rowell, EC Kent, A Kaplan (2003) Global analyses of sea surface temperature, sea ice, and night marine air temperature since the late nineteenth century J Geophys Res 108, doi:10.1029/2002JD002670

Roeckner E, G Baüml, L Bonaventura, R Brokopf, M Esch, M Giorgetta, S Hagemann et al (2003) The atmospheric general circulation model ECHAM5: Part 1: model description. Max-Planck-Institut für Meteorologie, MPI-Report 353, Hamburg

Saji NH, BN Goswami, PN Vinayachandran, T Yamagata (1999) A dipole mode in the tropical Indian Ocean. Nature 401:360–363

Saji NH, T Yamagata (2003) Possible impacts of Indian Ocean Dipole mode events on global climate. Clim Res 25:151–169

Santoso A, MH England, W Cai (2012) Impact of Indo-Pacific feedback interactions on ENSO dynamics diagnosed using ensemble climate simulations. J Clim 25:7743–7763

Schott FA, SP Xie, JP McCreary Jr (2009) Indian Ocean circulation and climate variability Rev Geophys 47, RG1002, doi:10.1029/2007RG000245

Shi L, HH Hendon, O Alves, JJ Luo, M Balmaseda, D Anderson (2012) How predictable is the Indian Ocean Dipole? Mon Weather Rev 140:3867–3884

Shinoda T, HH Hendon, MA Alexander (2004a) Surface and subsurface dipole variability in the Indian Ocean and its relation to ENSO. Deep Sea Res 51:619–635

Shinoda T, MA Alexander, HH Hendon (2004b) Remote response of the Indian Ocean to interannual SST variations in the tropical Pacific. J Clim 17:362–372

Shinoda T, W Han (2005) Influence of the Indian Ocean Dipole on atmospheric subseasonal variability. J Clim 18:3891–3909

889 Spencer H, RT Sutton, JM Slingo, JM Roberts, E Black (2005) The Indian Ocean climate and
890 dipole variability in the Hadley centre coupled GCMs. J Clim 18:2286–2307
891 Sprintall J, A Révelard (2014) The Indonesian throughflow response to Indo-Pacific climate
892 variability. J Geophys Res Oceans 119, 1161–1175, doi:10.1002/2013JC009533
893 Stuecker MF, A Timmermann, J Yoon, F-F Jin (2015) Tropospheric biennial oscillation
894 (TBO) indistinguishable from white noise, Geophys Res Lett 42:7785–7791
895 Stuecker MF, A Timmermann, F-F Jin, Y Chikamoto, W Zhang, AT Wittenberg, E Widiasih,
896 and S. Zhao (2017) Revisiting ENSO/Indian Ocean Dipole phase relationships,
897 Geophys Res Lett 44:2481–2492
898 Sun S, J Lan, Y Fang, Tana, X Gao (2015) A triggering mechanism for the Indian Ocean
899 dipoles independent of ENSO. J Clim 28:5063–5076
900 Suzuki R, SK Behera, S Iizuka, T Yamagata (2004) Indian Ocean subtropical dipole
901 simulated using a coupled general circulation model. J Geophys Res 109,
902 doi:10.1029/2003JC001974
903 Terray P, S Dominiak (2005) Indian Ocean sea surface temperature and El Nino and Southern
904 Oscillation: a new perspective. J Clim 18:1351–1368
905 Terray P, S Dominiak, P Delecluse (2005) Role of the southern Indian Ocean in the
906 transitions of the monsoon-ENSO system during recent decades. Clim Dyn 24:169–195
907 Terray P, F Chauvin, H Douville (2007) Impact of southeast Indian Ocean sea surface
908 temperature anomalies on monsoon-ENSO dipole variability in a coupled ocean-
909 atmosphere model. Clim Dyn 28:553–580
910 Terray P, K Kamala, S Masson, G Madec, AK Sahai, JJ Luo, T Yamagata (2012) The role of
911 the intra-daily SST variability in the Indian monsoon variability and monsoon-ENSO–
912 IOD relationships in a global coupled model. Clim Dyn 39:729–754
913 Terray P, S Masson, C Prodhomme, MK Roxy, KP Sooraj (2016) Impacts of Indian and

914 Atlantic oceans on ENSO in a comprehensive modeling framework. Clim Dyn
915 46:2507–2533
916 Timmermann R, H Goosse, G Madec, T Fichefet, C Ethe, V Duliere (2005) On the
917 representation of high latitude processes in the ORCA-LIM global coupled sea ice-
918 ocean model. Ocean Model 8(1–2):175–201
919 Tozuka T, JJ Luo, S Masson, T Yamagata (2007) Decadal modulations of the Indian Ocean
920 dipole in the SINTEX-F1 coupled GCM. J Clim 20:2881–2894
921 Ummenhofer CC, MH England, GA Meyers, PC McIntosh, MJ Pook, JS Risbey, A Sen
922 Gupta, and AS Taschetto (2009) What causes southeast Australia's worst droughts?
923 Geophys Res Lett, 36:L04706, doi:10.1029/2008GL036801
924 Valcke S (2006) OASIS3 user guide (prism_2-5). PRISM support initiative report No 3, 64 pp
925 Vecchi GA, DE Harrison (2000) Tropical Pacific sea surface temperature anomalies, El Niño
926 and equatorial westerly events. J Clim 13:1814–1830
927 Wallace JM, C Smith, Q Jiang Q (1990) Spatial patterns of ocean–atmosphere interaction in
928 the northern winter. J Clim 3:990–998
929 Wang X, C Wang (2014) Different impacts of various El Niño events on the Indian Ocean
930 Dipole. Clim Dyn 42:991–1005
931 Wang J, D Yuan (2015) Roles of western and eastern boundary reflections in the interannual
932 sea level variations during negative Indian Ocean Dipole events. J Phys Ocean
933 45:1804–1821
934 Wang H, R Murtugudde, A Kumar (2016) Evolution of Indian Ocean dipole and its forcing
935 mechanisms in the absence of ENSO. Clim Dyn, doi:10.1007/s00382-016-2977-y
936 Webster PJ, Moore AM, Loschnigg JP, Leben RR (1999) Coupled ocean–atmosphere
937 dynamics in the Indian Ocean during 1997–98. Nature 401:356–360
938 Webster PJ, Hoyos CD (2010) Beyond the spring barrier? Nature Geoscience 3:152–153

939 Wyrtki K (1985) Water displacements in the Pacific and the genesis of El Niño cycles. J
940 Geophys Res Oceans 90:7129–7132
941 Xie S-P, H Annamalai, F Schott, JP McCreary Jr. (2002) Origin and predictability of South
942 Indian Ocean climate variability, J Clim., 15:864–874
943 Yamagata T, SK Behera, JJ Luo, S Masson , MR Jury, SA Rao (2004) Coupled ocean-
944 atmosphere variability in the tropical Indian Ocean. Geophysical Monograph Series
945 (eds) Wang C, Xie S P and Carton JA 147, 414 pp
946 Yang Y, SP Xie, L Wu, Y Kosoka, NC Lau, GA Vecchi (2015) Seasonality and predictability
947 of the Indian Ocean Dipole mode: ENSO forcing and internal variability. J Clim
948 28:8021–8036
949 Yuan D, H Liu (2009) Long wave dynamics of sea level variations during Indian Ocean
950 dipole events. J Phys Oceanogr 39:1115–1132
951 Yuan DL and Coauthors (2011) Forcing of the Indian Ocean Dipole on the interannual
952 variations of the tropical Pacific Ocean: Roles of the Indonesian Throughflow. J Clim
953 24:3593–3608
954 Yu J, KM Lau (2004) Contrasting Indian Ocean SST variability with and without ENSO
955 influence: a coupled atmosphere-ocean GCM study. Meteor Atmos Phys 90, doi:
956 10.1007 /s00703-004-0094-7
957 Yu W, B Xiang, L Liu, N Liu (2005) Understanding the origins of interannual thermocline
958 variations in the tropical Indian Ocean. Geophys Res Lett 32:L24706,
959 doi:10.1029/2005GL024327
960 Zhang Q, J Gottschalk (2002) SST anomalies of ENSO and the Madden–Julian oscillation in
961 the equatorial Pacific. J Clim 15:2429–2445
962 Zhang Y, JR Norris, JM Wallace (1998) Seasonality of large scale atmosphere–ocean
963 interaction over the North Pacific. J Clim 11:2473–2481

964 Zhao M, HH Hendon (2009) Representation and prediction of the Indian Ocean dipole in the
965 POAMA seasonal forecast model. Quart J Roy Meteo Soc 135:337–352
966 Zhao YP, YL Chen, F Wang, XZ Bai, AM Wu (2009) Two modes of dipole events in tropical
967 Indian Ocean. Sci China Ser D-Earth Sci 52:369–381
968

969 **Figure Captions**

970

971 **Figure 1:** (a) September–November SST (shadings every 0.05 K) and 20°C isotherm
972 depth (20D; contours every 1 m; green/purple contours for shallow/deep thermocline)
973 anomalies regressed onto the normalized boreal fall (i.e., SON) IOD index from Saji et al.
974 (1999) for the 1979-2008 observations. (b) Same as (a) but for rainfall (shadings every 0.25
975 $mm.day^{-1}$) and 850-hPa wind (vectors; $m.s^{-1}$) anomalies. (c-d) and (e-f) Same as (a-b) but for
976 the CTL and the FTPC experiments, respectively. Anomalies that are not significant at the
977 90% confidence level according to a bootstrap test are masked. See Section 2.3 for details on
978 the bootstrap test.

979

980 **Figure 2:** (a) SST homogeneous map of the first leading MCA mode (MCA1) between
981 monthly SST and 20D anomalies during boreal fall (September to November) for the 1979-
982 2008 observations. (b-c) Same as (a) but for the CTL and FTPC experiments, respectively. (d-
983 f) and (g-i) Same as (a-c) but for the 20D mode derived from the SST–20D MCA1 and for the
984 USTR mode derived from the SST–USTR MCA1, respectively. Units are labeled on the
985 Figure. Summary statistics for the different MCA1s are given in Tables 1-3.

986

987 **Figure 3:** (a-d) IOD prediction patterns of SST (shadings every 0.5 K) and 20D (contours
988 every 1 K; green/purple contours for negative/positive coefficients and black contours for
989 nullity) from the IOD peak season at year 0 (SON(0)) back to the preceding boreal winter
990 (DJF(0)) for the observations. (e-h) and (i-l) Same as (a-d) but for the CTL and the FTPC,
991 respectively. The IOD prediction patterns are obtained by regressing the non-normalized 20D
992 EC time series derived from SST–20D MCA1 and averaged in SON(0) onto normalized
993 quarterly anomalies at the grid point scale from SON(0) back to DJF(0). Significance tested at

994 the 90% confidence level as in Fig. 1. Only significant IOD predictions are shown for 20D.
995 Significant IOD predictions are shown with black dots for SST.
996
997 **Figure 4:** Same as Fig. 3 but for the IOD prediction patterns derived from 200-hPa
998 velocity potential (shadings every 0.5 K) and 850-hPa zonal wind (contours every 1 K;
999 dotted/solid contours for negative/positive coefficients) anomalies. Only significant IOD
1000 predictions at the 90% confidence level are shown for 850-hPa zonal winds. IOD predictions
1001 significant at the 90% confidence level are shown with black dots for 200-hPa velocity
1002 potential.
1003
1004 **Figure 5:** (a) Autocorrelation in the monthly SST, 20D and USTR EC time series. (b-c)
1005 Same as (a) but for the CTL and the FTPC, respectively. (d) Cross-correlation between the
1006 three EC time series for the FTPC. The EC time series are computed by projecting the
1007 monthly anomalies over the equatorial IO (10°S–10°N) for each variable onto the
1008 corresponding singular vectors derived from SST–20D MCA1 for SST and 20D and from
1009 SST–USTR MCA1 for USTR.
1010
1011 **Figure 6:** Monthly SST (contours every 0.05 K; blue/red contours for SST
1012 cooling/warming and black contours for nullity), 20D (shadings every 1 K; cool/warm
1013 shadings for thermocline shoaling/deepening) and wind stress (vectors; Pascal) anomalies
1014 from (a) Sep(-1) to (o) Nov(0) regressed onto the normalized 20D EC time series from SST–
1015 20D MCA1 averaged during SON(0) for the FTPC experiment. Significance tested at the 90%
1016 confidence level as in Fig. 1. Only significant regression coefficients are shown for SST and
1017 20D. Significant regression coefficients are shown by thick black arrows for wind stress.
1018

Figure 7: Same as Fig. 6 but from (a) Dec(0) to (l) Nov(+1). The black box in panel b shows the domain used for computing the 20D index in Section 5.

Figure 8: (a) Regression of 5-day 20D anomalies area-averaged in the 2°S–2°N band from September to June onto monthly 20D anomalies in the eastern equatorial IO (box shown in Fig. 7b) during January in the FTPC experiment. (b) Same as (a) but with the monthly 20D index in February. (c-d) and (e-f) Same as (a-b) but for 5-day OLR and USTR anomalies, respectively. Positive/Negative OLR and USTR anomalies correspond to weakened/strengthened convection and westerly/easterly wind anomalies, respectively. Black contours show significant regression coefficients at the 90% confidence level tested as in Fig. 1.

Figure 9: Lead/lag pentad correlations between 20D anomalies area-averaged in the eastern equatorial IO (box in Fig. 7b) and zonal IO anomalies in (a-c) 20D, (d-f) USTR and (g-i) OLR averaged in the band 2°S-2°N for the FTPC experiment. Time series of both 20D index and climate zonal anomalies span 13 pentads. The 20D index is fixed and centered onto Dec 15, while climate zonal anomalies slide from 12 pentads ahead to 12 pentads after Dec 15, every 1 pentad. Lag 0 corresponds to the synchronous correlation (i.e., centered onto Dec 15). The direction of the lead/lag relationship is labeled on each panel. First, second and third columns correspond to lead/lag correlations averaged over the entire simulation period and for years following the 10% most intense pIODs and nIODs, respectively. The 10% most intense p/nIODs events are defined when the 20D EC time series (derived from SST–20D MCA1) averaged during SON is below/above its 10^{th}/90^{th} percentile threshold value. Significance is computed for each year at the 90% confidence level according to the Bravais-Pearson test.

Light-to-dark contours show significant correlations reached 50% to 90% of the years, every 10%.

Figure 10: (a-b) Monthly evolution of 20D anomalies (m), area-averaged in the eastern equatorial IO (box in Fig. 7b), one year back to the occurrence of pIODs and nIODs, respectively. (c-d) Same as (a-b) but one year after p/nIODs. Thin curves represent the 20D evolution of the 10% most intense IOD events (see Fig. 9 for definition) and thick curve is the ensemble mean.

Figure 11: Regression of quarterly SLP (contours every 10 Pa, blue/red contour for low/high pressure and black contour for nullity), 200-hPa velocity potential (shadings every 1 x 10^4 $m^2.s^{-1}$; cold/warm colors for upper-level divergence/convergence) and 850-hPa wind (vectors; $m.s^{-1}$) anomalies regressed from (a) SON(-1) to (e) SON(0) onto the normalized 20D EC time series (derived from the SST–20D MCA1) in SON(0) for the FTPC experiment. Regression coefficients that are not significant at the 90% confidence level according to a bootstrap test are masked for SLP and 200-hPa velocity potential. Significant regression coefficients are shown by thick black arrows for 850-hPa wind.

Figure 12: Same as Fig. 11 but for the regressions of 20D (shadings) and SST (contours) anomalies. Regression coefficients that are not significant at the 90% confidence level according to a bootstrap test are masked for SST. Significant 20D anomalies at the 90% confidence level are shown with black dots.

Table Captions

Table 1: Summary statistics for the first SST–USTR MCA leading mode (MCA1) applied onto 10°S–10°N monthly anomalies during boreal fall (September to November) in the observations and the two experiments.

Table 2: Same as Table 1 but for the SST–20D MCA1.

Table 3: Same as Table 1 but for the 20D–USTR MCA1.

Tables

	SFC (%)	NC (%)	r inter-EC: SST – USTR	SSTvar (%)	USTRvar (%)	r EC – IOD Saji		r EC – IOD SINTEX	
						SST	USTR	SST	USTR
OBS	92.7	29.53	0.68	44.48	41.78	0.88	0.85	/	/
CTL	91.78	26.11	0.74	39.82	31.46	0.86	0.78	0.90	0.83
FTPC	79.13	22.25	0.69	33.99	30.77	0.78	0.65	0.84	0.71

The SCF gives the fraction of the square covariance between SST and USTR explained by MCA1. The NC and inter-EC correlation (r) assess the strength of the SST–USTR coupling. SSTvar and USTRvar are the variance of SST and USTR explained by their respective expansion coefficient (EC) time series. The correlation r between each EC time series and the IOD as defined by Saji et al. (1999), both averaged during SON, quantifies how well MCA1 summarizes the IOD variability. Similar r correlation is computed for the two experiments but with the 5°S–5°N band removed from the western IO box of the IOD domain to exclude the strong intrusion of the eastern equatorial cold tongue in the western IO simulated by the SINTEX model. See Sections 2.3 and 3.2 for details.

Table 1: Summary statistics for the first SST–USTR MCA leading mode (MCA1) applied onto 10°S–10°N monthly anomalies during boreal fall in the observations and the two experiments.

	SFC (%)	NC (%)	r inter-EC: SST – 20D	SSTvar (%)	20Dvar (%)	r EC – IOD Saji		r EC – IOD SINTEX	
						SST	20D	SST	20D
OBS	86.17	24.03	0.79	45.20	20.61	0.88	0.93	/	/
CTL	97.84	38.50	0.87	40.82	47.35	0.84	0.78	0.88	0.83
FTPC	95.41	34.57	0.85	35.26	46.45	0.77	0.71	0.84	0.78

Table 2: Same as Table 1 but for the SST–20D MCA1.

	SFC (%)	NC (%)	r inter-EC: 20D – USTR	20Dvar (%)	USTRvar (%)	r EC – IOD Saji		r EC – IOD SINTEX	
						20D	USTR	20D	USTR
OBS	88.01	24.08	0.80	21.72	41.31	0.91	0.86	/	/
CTL	95.65	30.13	0.77	47.28	32.19	0.78	0.77	0.83	0.82
FTPC	94.71	28.45	0.74	46.27	31.68	0.71	0.64	0.77	0.71

Table 3: Same as Table 1 but for the 20D–USTR MCA1.

Figures

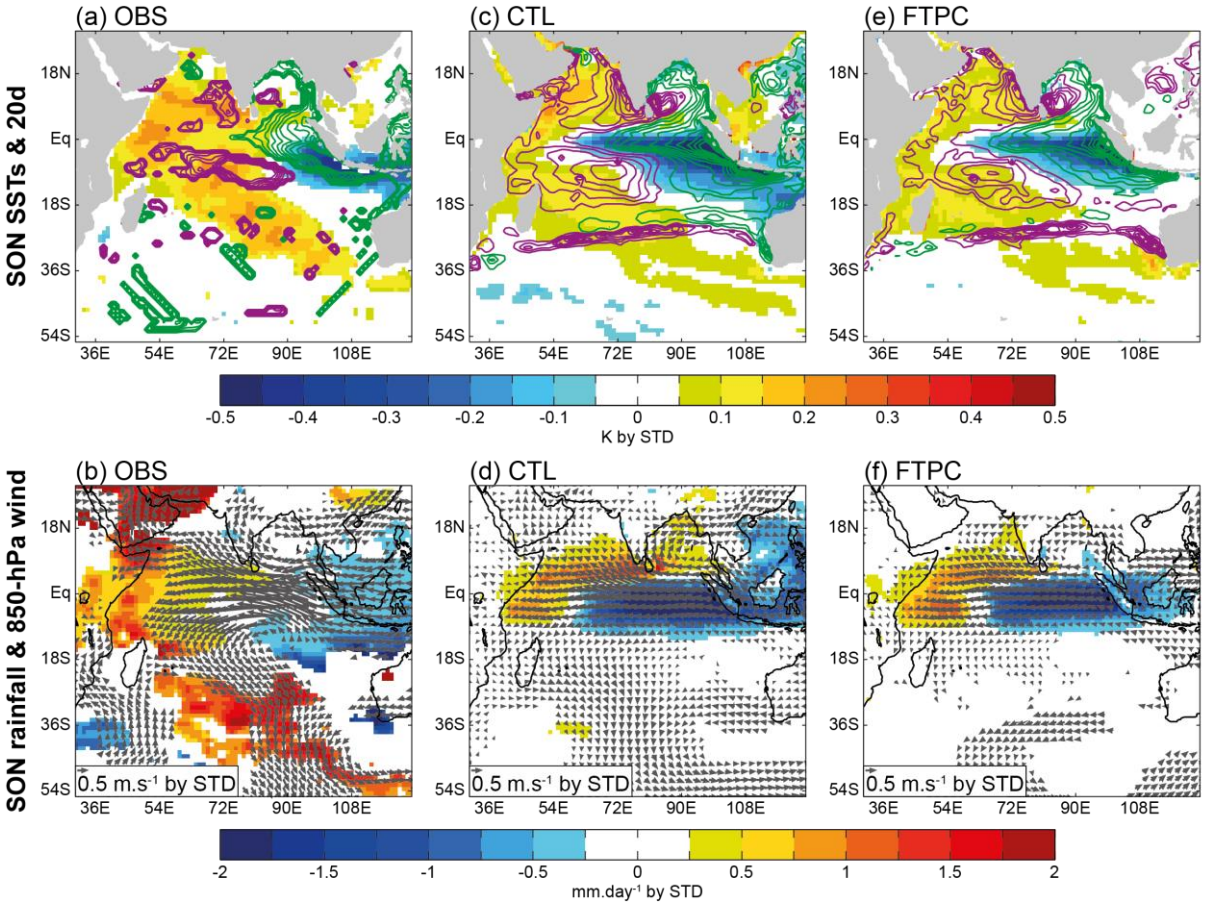

Figure 1: (a) September–November SST (shadings every 0.05 K) and 20°C isotherm depth (20D; contours every 1 m; green/purple contours for shallow/deep thermocline) anomalies regressed onto the normalized boreal fall (i.e., SON) IOD index from Saji et al. (1999) for the 1979-2008 observations. (b) Same as (a) but for rainfall (shadings every 0.25 mm.day^{-1}) and 850-hPa wind (vectors; m.s^{-1}) anomalies. (c-d) and (e-f) Same as (a-b) but for the CTL and the FTPC experiments, respectively. Anomalies that are not significant at the 90% confidence level according to a bootstrap test are masked. See Section 2.3 for details on the bootstrap test.

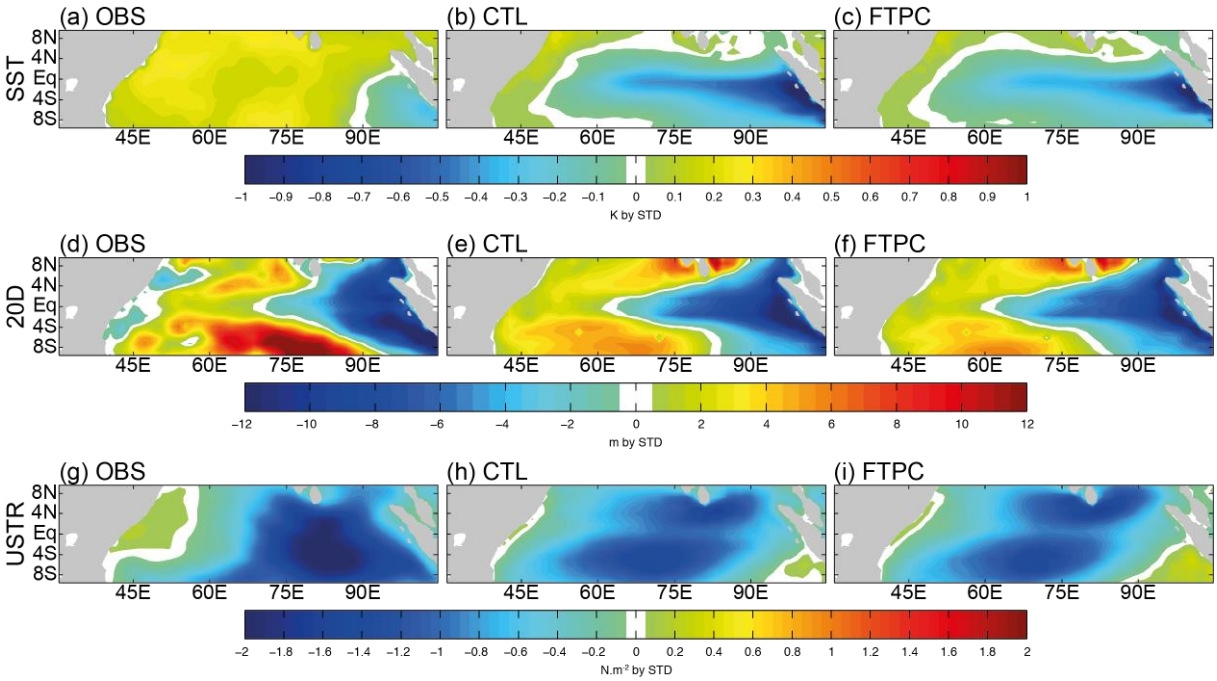

Figure 2: (a) SST homogeneous map of the first leading MCA mode (MCA1) between monthly SST and 20D anomalies during boreal fall (September to November) for the 1979-2008 observations. (b-c) Same as (a) but for the CTL and FTPC experiments, respectively. (d-f) and (g-i) Same as (a-c) but for the 20D mode derived from the SST–20D MCA1 and for the USTR mode derived from the SST–USTR MCA1, respectively. Units are labeled on the Figure. Summary statistics for the different MCA1s are given in Tables 1-3.

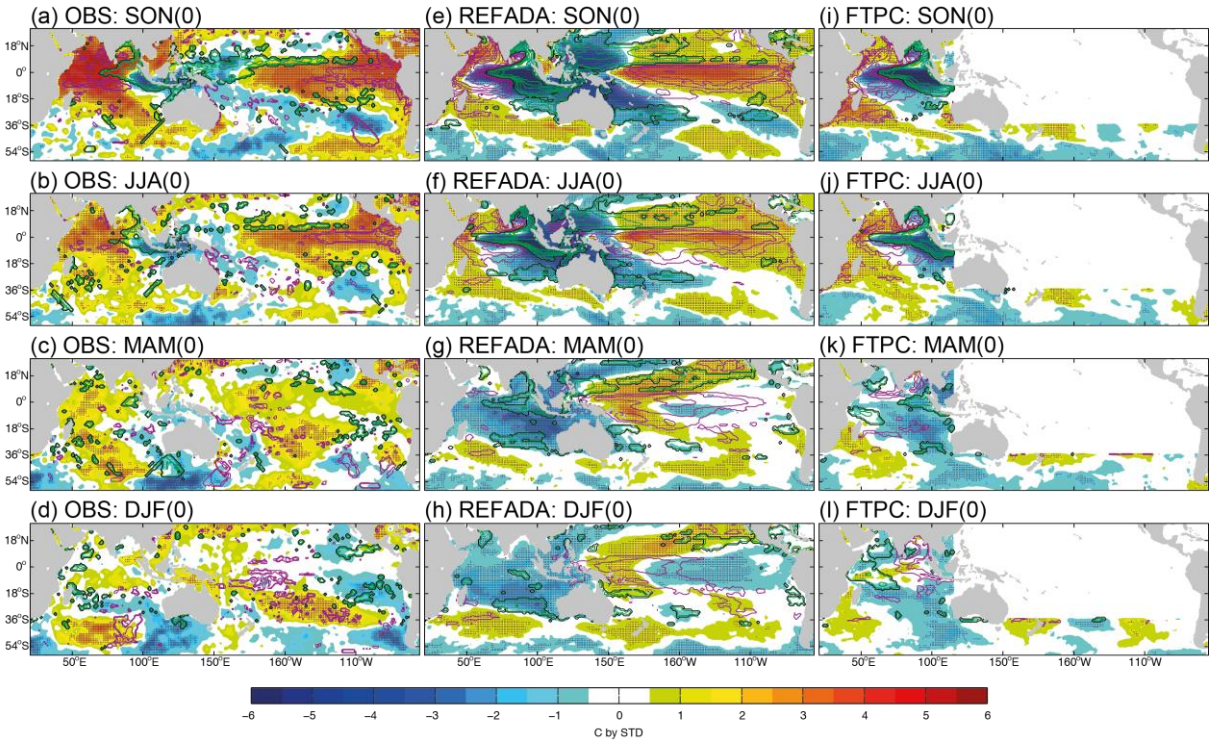

Figure 3: (a-d) IOD prediction patterns of SST (shadings every 0.5 K) and 20D (contours every 1 K; green/purple contours for negative/positive coefficients and black contours for nullity) from the IOD peak season at year 0 (SON(0)) back to the preceding boreal winter (DJF(0)) for the observations. (e-h) and (i-l) Same as (a-d) but for the CTL and the FTPC, respectively. The IOD prediction patterns are obtained by regressing the non-normalized 20D EC time series derived from SST–20D MCA1 and averaged in SON(0) onto normalized quarterly anomalies at the grid point scale from SON(0) back to DJF(0). Significance tested at the 90% confidence level as in Fig. 1. Only significant IOD predictions are shown for 20D. Significant IOD predictions are shown with black dots for SST.

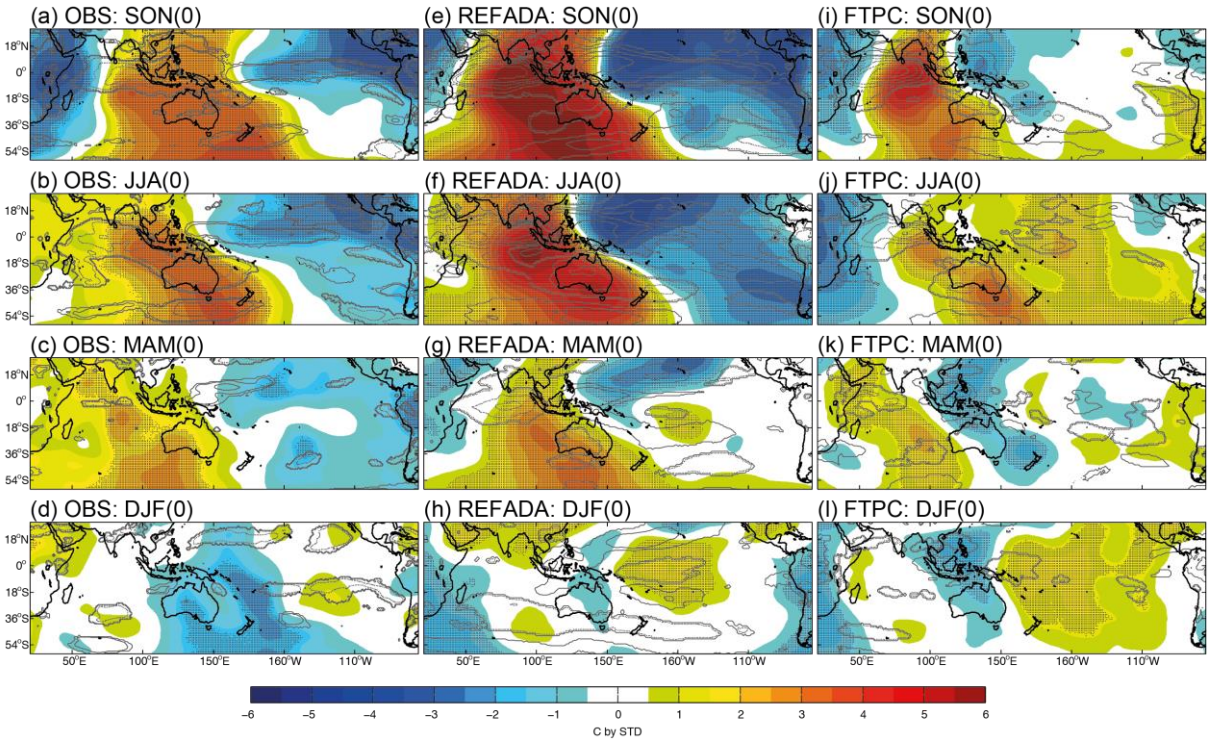

Figure 4: Same as Fig. 3 but for the IOD prediction patterns derived from 200-hPa velocity potential (shadings every 0.5 K) and 850-hPa zonal wind (contours every 1 K; dotted/solid contours for negative/positive coefficients) anomalies. Only significant IOD predictions at the 90% confidence level are shown for 850-hPa zonal winds. IOD predictions significant at the 90% confidence level are shown with black dots for 200-hPa velocity potential.

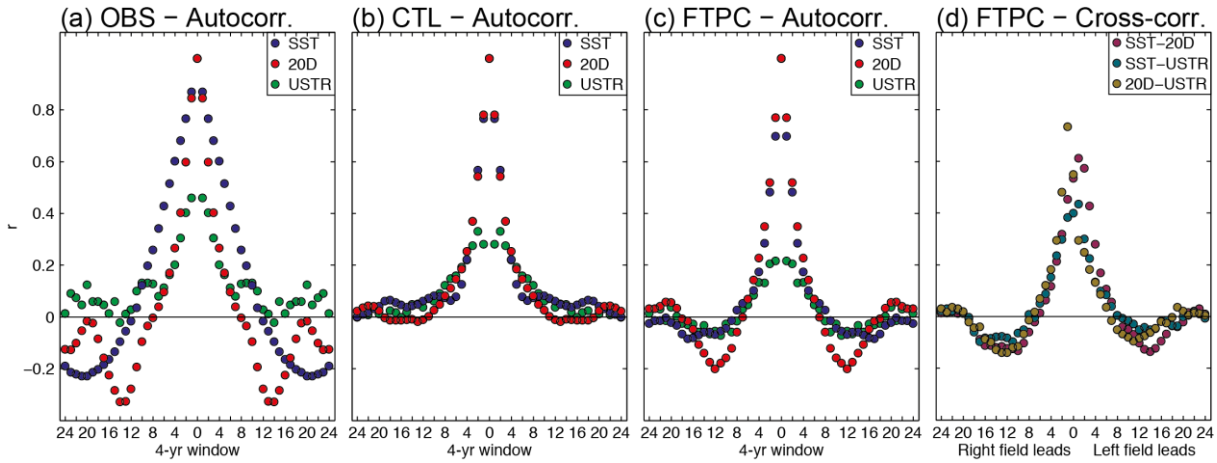

Figure 5: (a) Autocorrelation in the monthly SST, 20D and USTR EC time series. (b-c) Same as (a) but for the CTL and the FTPC, respectively. (d) Cross-correlation between the three EC time series for the FTPC. The EC time series are computed by projecting the monthly anomalies over the equatorial IO (10°S–10°N) for each variable onto the corresponding singular vectors derived from SST–20D MCA1 for SST and 20D and from SST–USTR MCA1 for USTR.

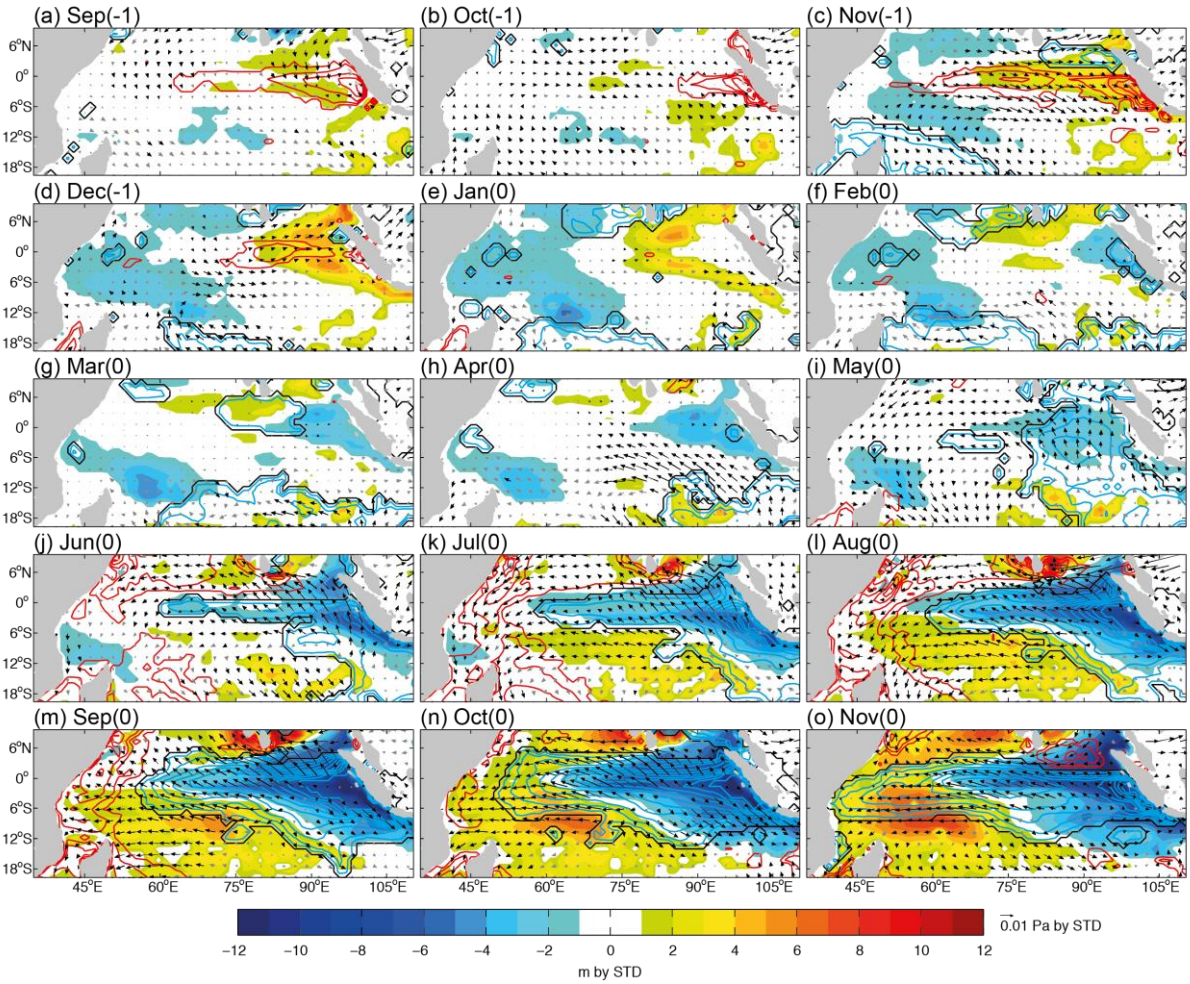

Figure 6: Monthly SST (contours every 0.05 K; blue/red contours for SST cooling/warming and black contours for nullity), 20D (shadings every 1 K; cool/warm shadings for thermocline shoaling/deepening) and wind stress (vectors; Pascal) anomalies from (a) Sep(-1) to (o) Nov(0) regressed onto the normalized 20D EC time series from SST–20D MCA1 averaged during SON(0) for the FTPC experiment. Significance tested at the 90% confidence level as in Fig. 1. Only significant regression coefficients are shown for SST and 20D. Significant regression coefficients are shown by thick black arrows for wind stress.

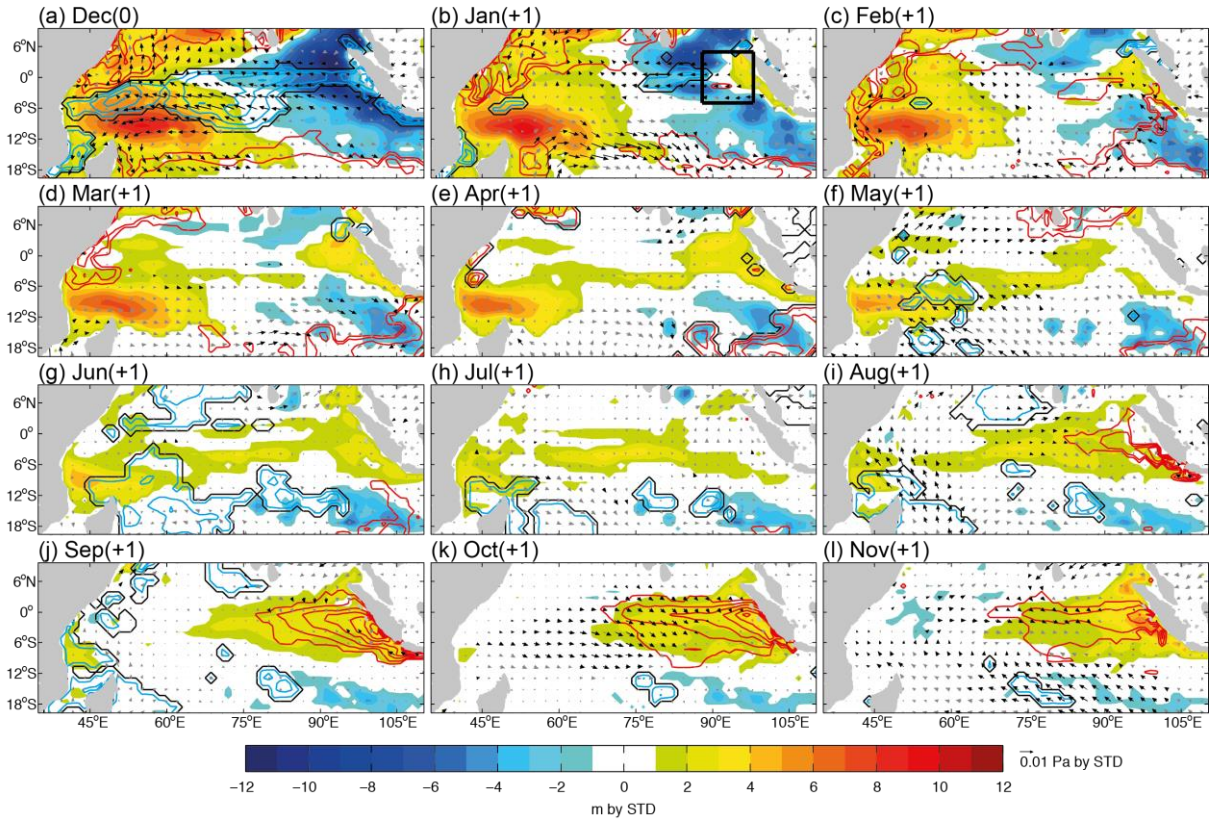

Figure 7: Same as Fig. 6 but from (a) Dec(0) to (l) Nov(+1). The black box in panel b shows the domain used for computing the 20D index in Section 5.

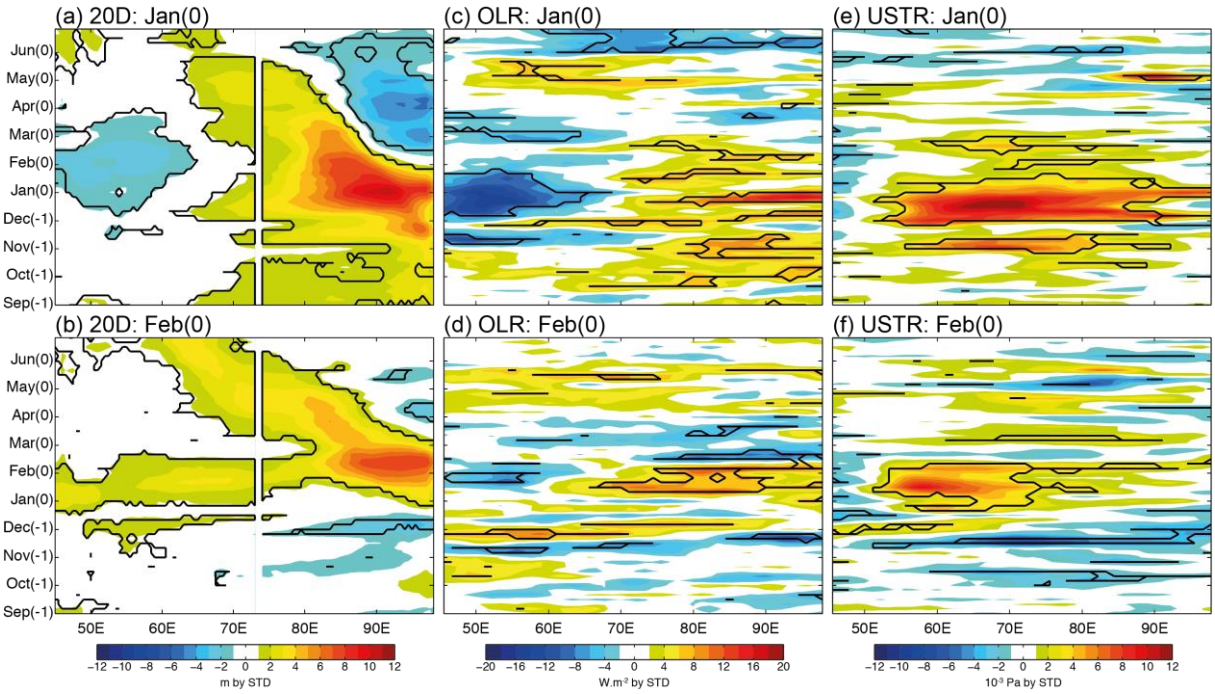

Figure 8: (a) Regression of 5-day 20D anomalies area-averaged in the 2°S–2°N band from September to June onto monthly 20D anomalies in the eastern equatorial IO (box shown in Fig. 7b) during January in the FTPC experiment. (b) Same as (a) but with the monthly 20D index in February. (c-d) and (e-f) Same as (a-b) but for 5-day OLR and USTR anomalies, respectively. Positive/Negative OLR and USTR anomalies correspond to weakened/strengthened convection and westerly/easterly wind anomalies, respectively. Black contours show significant regression coefficients at the 90% confidence level tested as in Fig. 1.

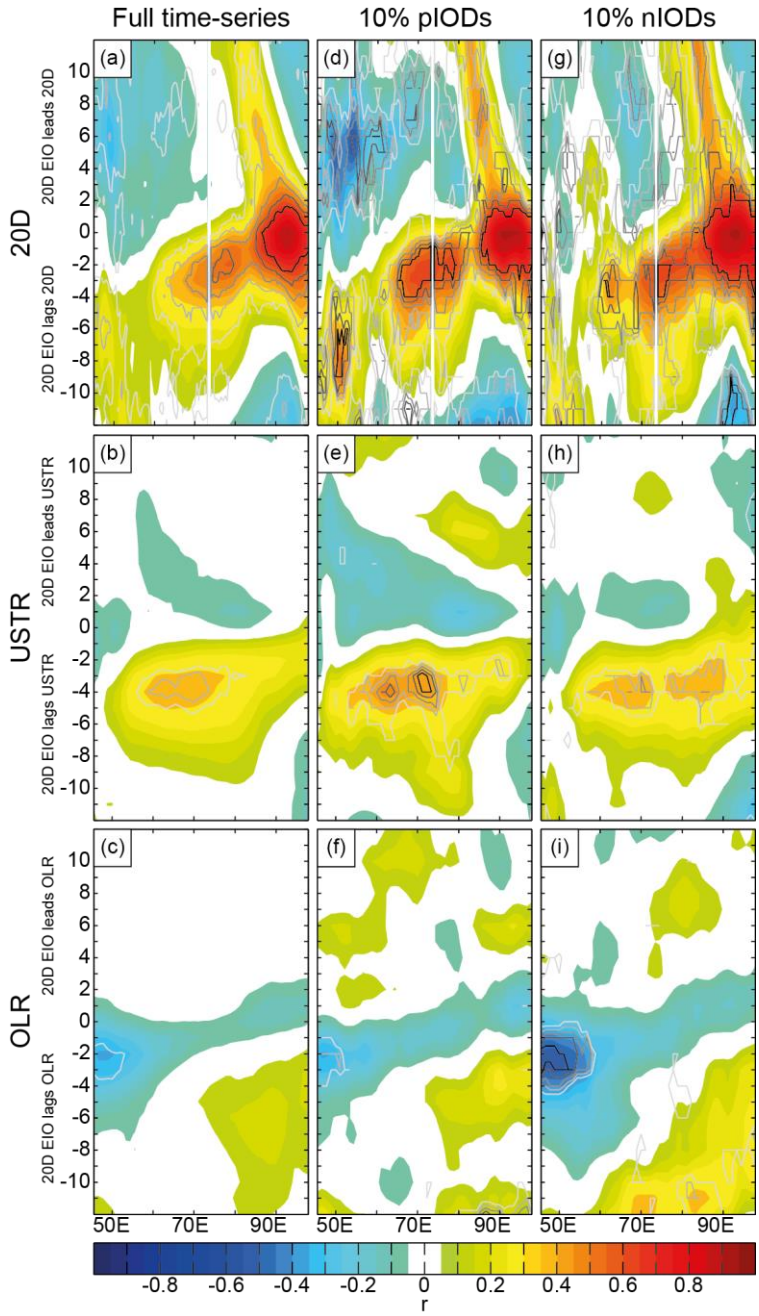

Figure 9: Lead/lag pentad correlations between 20D anomalies area-averaged in the eastern equatorial IO (box in Fig. 7b) and zonal IO anomalies in (a-c) 20D, (d-f) USTR and (g-i) OLR averaged in the band 2°S-2°N for the FTPC experiment. Time series of both 20D index and climate zonal anomalies span 13 pentads. The 20D index is fixed and centered onto Dec 15, while climate zonal anomalies slide from 12 pentads ahead to 12 pentads after Dec 15, every 1 pentad. Lag 0 corresponds to the synchronous correlation (i.e., centered onto Dec 15). The direction of the lead/lag relationship is labeled on each panel. First, second and third columns correspond to lead/lag correlations averaged over the entire simulation period and for years following the 10% most intense pIODs and nIODs, respectively. The 10% most intense p/nIODs events are defined when the 20D EC time series (derived from SST–20D MCA1) averaged during SON is below/above its 10^{th}/90^{th} percentile threshold value. Significance is computed for each year at the 90% confidence level according to the Bravais-Pearson test. Light-to-dark contours show significant correlations reached 50% to 90% of the years, every 10%.

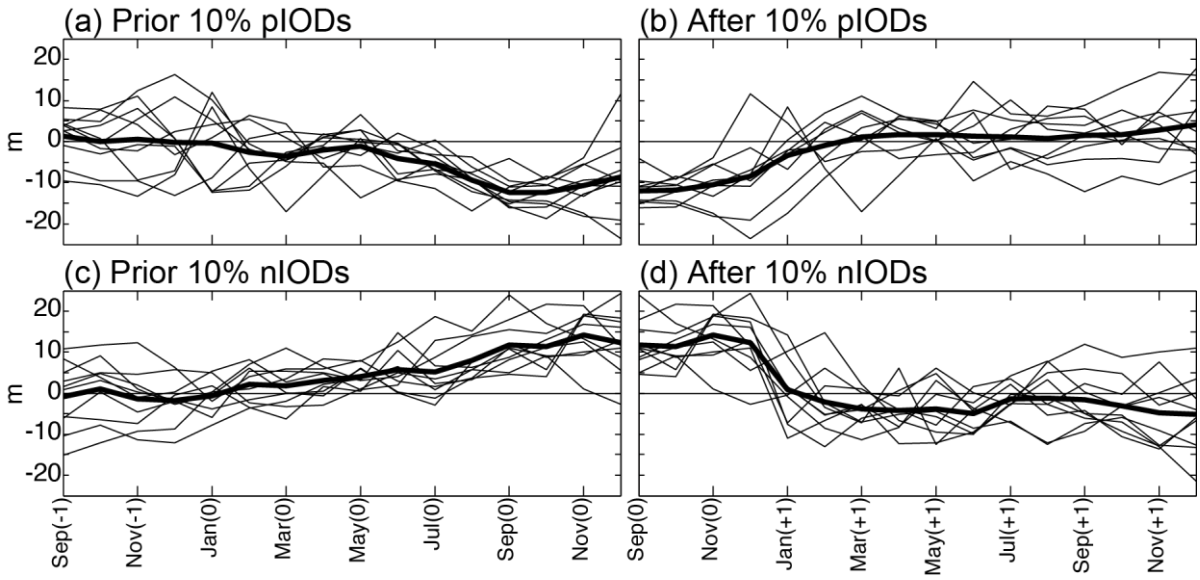

Figure 10: (a-b) Monthly evolution of 20D anomalies (m), area-averaged in the eastern equatorial IO (box in Fig. 7b), one year back to the occurrence of pIODs and nIODs, respectively. (c-d) Same as (a-b) but one year after p/nIODs. Thin curves represent the 20D evolution of the 10% most intense IOD events (see Fig. 9 for definition) and thick curve is the ensemble mean.

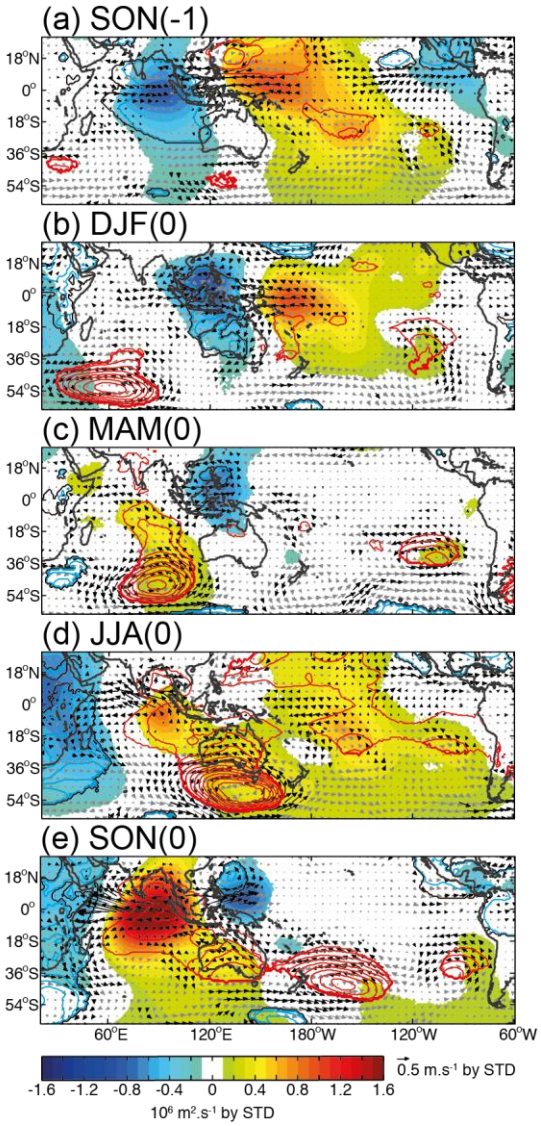

Figure 11: Regression of quarterly SLP (contours every 10 Pa, blue/red contour for low/high pressure and black contour for nullity), 200-hPa velocity potential (shadings every 1 x 10^4 $m^2.s^{-1}$; cold/warm colors for upper-level divergence/convergence) and 850-hPa wind (vectors; $m.s^{-1}$) anomalies regressed from (a) SON(-1) to (e) SON(0) onto the normalized 20D EC time series (derived from the SST–20D MCA1) in SON(0) for the FTPC experiment. Regression coefficients that are not significant at the 90% confidence level according to a bootstrap test are masked for SLP and 200-hPa velocity potential. Significant regression coefficients are shown by thick black arrows for 850-hPa wind.

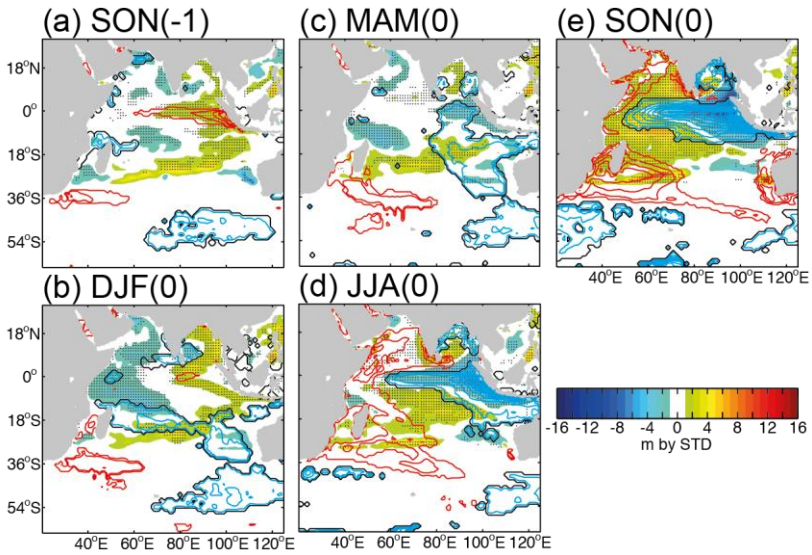

Figure 12: Same as Fig. 11 but for the regressions of 20D (shadings) and SST (contours) anomalies. Regression coefficients that are not significant at the 90% confidence level according to a bootstrap test are masked for SST. Significant 20D anomalies at the 90% confidence level are shown with black dots.